This is a non-peer-reviewed preprint submitted to EarthArXiv.
The manuscript is currently under review at *Communications Earth & Environment.*

Two-thirds of global coastline affected by climate-driven saline groundwater intrusion by end of century, reaching far inland by 2300

Daniel V. Kretschmer
Corresponding author: Institute of Geography, Johannes Gutenberg-University Mainz, Mainz, Germany;
Institute of Environmental Science and Geography, University of Potsdam, Potsdam, Germany;
dkretsch@uni-mainz.de

Kevin M. Befus
Department of Geosciences, University of Arkansas, Fayetteville, Arkansas, USA; kmbefus@uark.edu

Holly A. Michael
Department of Earth Sciences, University of Delaware, Newark, Delaware, USA; hmichael@udel.edu

Nils Moosdorf
Department for Biogeochemistry / Geology, Leibniz Centre for Tropical Marine Research (ZMT), Bremen, Germany;
Institute of Geosciences, University of Kiel, Kiel, Germany;
nils.moosdorf@leibniz-zmt.de

Gualbert H. P. Oude Essink
Department of Groundwater and Water Security, Deltares, Utrecht, The Netherlands;
Department of Physical Geography, Utrecht University, Utrecht, Netherlands;
gualbert.oudeessink@deltares.nl

Marc F. P. Bierkens
Department of Physical Geography, Utrecht University, Utrecht, The Netherlands;
Department of Groundwater and Water Security, Deltares, Utrecht, The Netherlands;
m.f.p.bierkens@uu.nl

Thorsten Wagener
Institute of Environmental Science and Geography, University of Potsdam, Potsdam, Germany;
thorsten.wagener@uni-potsdam.de

Robert Reinecke
Institute of Geography, Johannes Gutenberg-University Mainz, Mainz, Germany;
Institute of Environmental Science and Geography, University of Potsdam, Potsdam, Germany;
reinecke@uni-mainz.de

<u>Corresponding author</u>: Daniel V. Kretschmer (dkretsch@uni-mainz.de)

Abstract (150 words)

Fresh groundwater is a vital resource along global coastlines where already over a third of the world's population lives. Saline groundwater intrusion, driven by sea-level rise, groundwater abstraction, and reduced recharge, threatens the potability of coastal groundwater. Yet, the global potential for intrusion remains uncertain. Using a global groundwater model, we assess climate-driven saline groundwater intrusion along global coastlines until 2300 under a mild climate-change scenario. We find that two-thirds of the coastline will be affected by climate-driven intrusion of shallow groundwater between 2025 and 2100, and that it can locally intrude more than 9 km inland by 2300. While topography, aquifer thickness, and porosity define saline groundwater reach, climate-driven intrusion is mainly controlled by hydraulic conductivity and sea-level rise. We assess risk by combining intrusion, coastal populations, and groundwater use. Most populated coastlines will face a moderate risk, with high risk in the Mediterranean and South and East Asia.

Main

Over 2.5 billion people live in the global coastal zone (within 100 km of the coastline)[1], where groundwater is a key freshwater supply. Used for irrigation and public water supply, coastal groundwater is the primary source of freshwater in coastal counties in the United States[2], coastal megacities like Shanghai and Buenos Aires[3], and even entire countries, as reported for Small Island Nations[4]. This dependence on groundwater, combined with increasing withdrawals[5], has already led to a rapid decline in global coastal groundwater levels[6]. Longer, more intense droughts due to climate change, which make surface water availability inconsistent[7], are expected to further increase dependence on groundwater as a more reliable freshwater source. Meanwhile, the availability and reliability of both surface water and groundwater are expected to decline due to sea-level rise[8,9] and regional changes in recharge[10]. As the population in low-elevation coastal zones (i.e., up to 10 m elevation) is projected to rise from 0.6 to 1.3 billion people between 2000 and 2060[11], fresh coastal groundwater will become increasingly stressed.

The availability of freshwater along coasts is threatened by the intrusion of saline groundwater into coastal aquifers, which has already been reported in multiple regions worldwide[12,13,14]. Thus, coastal populations depending on groundwater abstraction (e.g., to irrigate crops) are highly vulnerable to changes in this resource[15,16]. Saline water intrudes aquifers where coastal hydraulic gradients decline[17,18], potentially rendering the water unusable for irrigation or drinking[19]. Drivers of saline groundwater intrusion include declining groundwater tables (due to, e.g., groundwater pumping and reduced groundwater recharge) and rising sea levels[20]. Exposure to saline groundwater intrusion has been reported as a major problem in highly populated regions, with approximately one-third of all coastal metropolises already having saline groundwater intrusion problems[21].

Globally, the intrusion of saline groundwater into coastal aquifers is expected to intensify in areas with reductions in groundwater recharge and rising sea levels. Based on SSP1-2.6 (shared socio-economic pathway with medium adaptive capacity)[22] groundwater recharge is estimated to reduce by 30% (2050-2080 vs. 1980-2010) in the large coastal areas of the Mediterranean, Central America, South America and Australia[10]. In addition, rising sea levels are expected to reduce the freshwater coastal groundwater resources that supply roughly 8 million people (based on RCP2.6) and up to 60 million people (based on RCP 8.5) worldwide by approximately 5% by the year 2100[9].

Although climate change will likely reduce the availability of fresh coastal groundwater, we currently have limited long-term historical records of groundwater salinity and lack projections beyond the year 2100[23]. Recent modelling studies have identified steep topography as a setting that can limit saline groundwater intrusion[9,24]. Coastal aquifers are considered highly resilient against saline groundwater intrusion, where both high hydraulic gradients towards the coastline and an unsaturated zone (i.e., to accommodate increasing groundwater levels which balance rising sea-level) exist[25]. However, we lack understanding of the globally distributed risk emerging from saline groundwater intrusion in the context of the population exposed and their dependence on fresh groundwater[7] (see Methods).

To gain a deeper understanding of saline groundwater intrusion, we simulate global climate-driven (i.e., driven by anthropogenic climate change) saline groundwater intrusion incorporating changes in sea level and groundwater recharge from 1861 to the year 2300. The spatial resolution is 5 arcmin, and the temporal resolution is 1 year (see the Methods section, Text S1, S2, and Figure S1, S2). The initial condition of the transient simulation is generated by a 485,000-year long-term equilibrium simulation (see Text S3 and Figure S3). Using an equilibrium as initial condition, likely overestimating initial coastal groundwater salinity, but allows to assess changes induced by projected climate change isolated from historic influences[26]. Climate change is represented as changes in groundwater recharge, based on an ensemble mean of eight global hydrological models[27], and sea-level rise[28,29]. The applied sea-level rise and groundwater recharge change projections represent the socioeconomic path RCP 2.6, which was chosen since it provides a conservative estimate of climatic changes and consistent model simulations are available as forcing till 2300[7]. In contrast to a recent assessment simulating intrusion till 2100[9], we also simulate entire continents rather than simplified representative cross-sections along the near-global coastline. The main advantages of simulating entire continents are that no assumptions about inland boundary conditions need to be made, which can strongly impact simulations of saline groundwater intrusion[18], and that the global distribution of geographic and hydrogeologic features is simulated (e.g., the model also simulates the interaction to surface water bodies). The presented first global simulation results of climate-driven saline groundwater intrusion are then used to assess future risks emerging from saline groundwater intrusion and which factors control the process.

We forecast risk in climate reference regions around the globe (see Text S4 and Table S1)[30] by aggregating the hazard of climate-driven saline groundwater intrusion, exposed population[31] and vulnerability due to net abstraction[27]. To better understand which physical features control climate-driven saline groundwater intrusion at the global scale, we analyze model sensitivities. A random forest algorithm is used to determine the most important physical features, and which parameter ranges make a location susceptible to climate-driven saline groundwater intrusion[32].

Climate change is increasing saline groundwater intrusion risk

We forecast that two thirds of the global coastline will be affected by climate-driven saline groundwater intrusion between 2025 and 2100. Little additional expansion of the affected coastline is projected over the following two centuries with 69% by 2200 and 72% by 2300. While 75% of climate-driven saline groundwater intrusion volume by 2300 occurred in model cells along the coastline, 25% of the intruded volume is forecasted in model cells 5 arcmin inland (~9.3 km at the Equator). In the period from 2025 to 2300, we forecast the global volume of climate-driven saline groundwater intrusion to be 108.21 km^3.

The highest saline groundwater intrusion volumes (> 5 km^3) from 2025 to 2300 are simulated for the Mediterranean (MED), South East Asia (SEA), North-West North-America (NWN), North South-America (NSA) and the Russian Arctic (RAR) (see Figure 1). Meanwhile, climate-driven saline groundwater intrusion per unit length of coastline of over 0.5 m^3/m is projected in North South-America (NSA), North-East South-America (NES), and South-East South-America (SES) (see Figure S4). The largest forecasted regional shares of coastline area with saline groundwater intrusion between 2025 and 2300 are 85% in Central North America (CNA), 83% in East Australia (EAU), and 77% in Central Australia (CAU). The distribution of model cells across climate reference regions is shown in Figure S5.

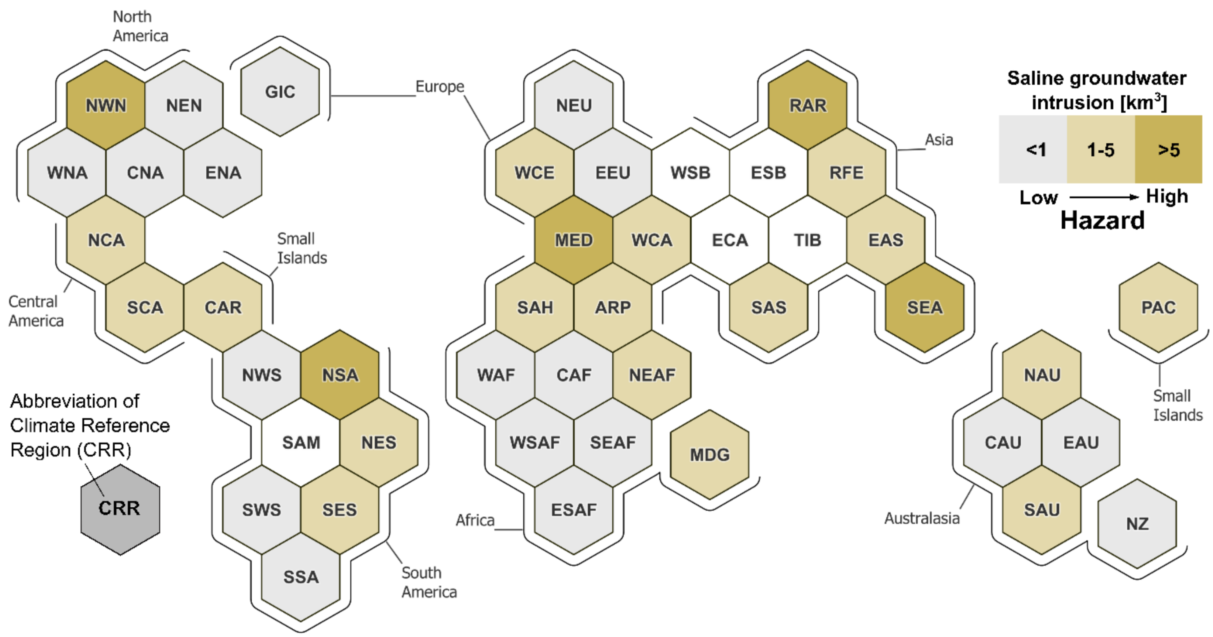

Figure 1 – Simulated climate-driven saline groundwater intrusion between 2025 and 2300, aggregated for each climate reference region (for list of abbreviations, see Table S1). The abbreviations for the most commonly referred to regions discussed are Mediterranean (MED) and South East Asia (SEA). White regions are landlocked. Hexagons adapted from ref. [22].

We find the highest risk of climate-driven saline groundwater intrusion by 2300 in MED, South Asia (SAS), and East Asia (EAS), where high saline groundwater intrusion, population and groundwater dependence coincide (see Figure 2). We calculate the risk for each climate reference region by aggregating saline groundwater intrusion hazard, population exposure[31] and vulnerability due to groundwater abstraction simulated using the hydrologic model WaterGAP[27]. Hazard, exposure and vulnerability are summed within climate reference regions, their sums are then normalized, and the norms multiplied with each other resulting in the final risk value (see Methods). Due to high groundwater abstraction and large population, the risk in MED, SAS, and EAS is higher than in SEA, which is the climate reference region with the highest simulated saline groundwater intrusion by 2300 (17.7 km^3). Meanwhile, risk decreases in North-East America (NEN) and Greenland/Iceland (GIC) throughout the simulated period due to reduced relative sea levels (projected to reach -0.37 m and -1.53 m until 2300, respectively, see Text S5). Besides NEN and GIC, risk is lowest in South South-America (SSA), East Europe (EEU), Russian Arctic (RAR), Russian Far-East (RFE), SEA and Central Australia (CAU).

Large hazards of climate-driven saline groundwater intrusion (see Figure 1) and populations exposed (see Figure S6) are found in MED and SEA, while MED is the only region that also has high vulnerability (see bivariate plots of hazard with exposure, and hazard with vulnerability in Figure 2b and 2c). A small hazard combined with high exposure and high vulnerability (see Figure S7) are found in East North-America (ENA) and North Europe (NEU). Meanwhile, a large hazard combined with low exposure and low vulnerability is found in the RAR. Three regions have low values in hazard, exposure, and vulnerability: EEU, NEN, and SSA.

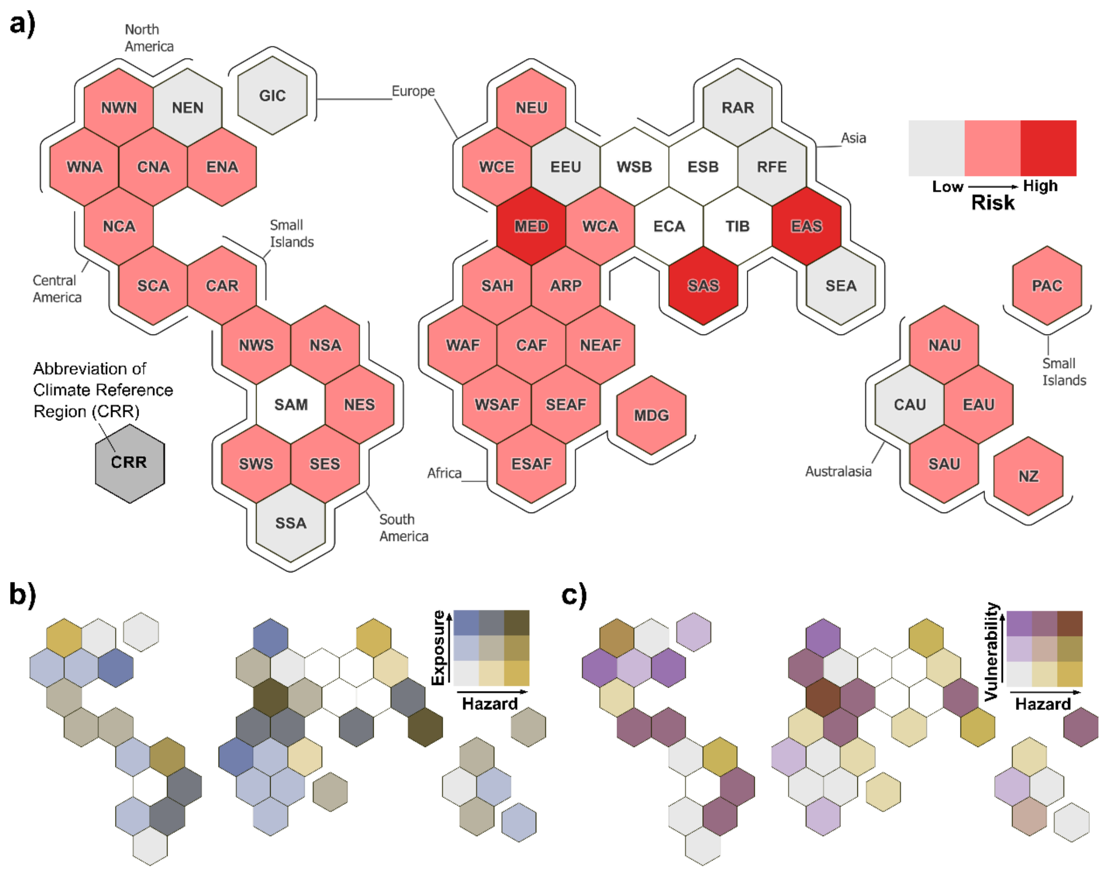

Figure 2 – Risk of climate change-driven saline groundwater intrusion in climate reference regions (for list of abbreviations, see Table S1). White regions are landlocked. The subplots show a) risk by 2300 (vs. 2025), b) hazard (saline groundwater intrusion) by 2300 (vs. 2025) and exposure (estimated population count in 2020[31]), c) hazard (saline groundwater intrusion) by 2300 (vs. 2025) and vulnerability (estimated net annual groundwater abstraction mean for 2007-2016[27]). Hexagons adapted from ref. [22], bivariate plots also shown in Figures S8 and S9.

While sea-level rise drives climate-driven saline groundwater intrusion, hydraulic conductivity controls aquifer susceptibility

We assess the model's sensitivities, using a random forest algorithm and the PAWN method (see Methods section, Text S6 and Figure S15), to determine driver (i.e., sea-level rise, groundwater recharge change) and physical feature importance in climate-driven saline groundwater intrusion. The random forest feature importance measures how important a feature is in splitting samples into groups with minimum Gini impurity. Here, 1000 samples of all model cells are split into groups with mostly increasing salinity and with mostly reducing salinity driven by climate change. For each sample split, the feature threshold gets stored at which the minimum Gini impurity is found. We use the median of thresholds in all random forest trees (i.e., 1000 trees) to derive the susceptibility thresholds for the physical features.

Figure 3 shows the feature importances (grey boxes) and susceptibility thresholds (colored lines) for climate-driven saline groundwater intrusion derived using the random forest algorithm. We find that, the main driver of simulated saline groundwater intrusion is sea-level rise, with groundwater recharge change being secondary. While sea-level rise is the main driver, the feature importance of hydraulic conductivity exceeds that of sea-level rise (see Figure 3). This means that in regions with rising sea levels, hydraulic conductivity controls whether climate-driven saline groundwater intrusion occurs or not.

From 2000 to 2300, the importance of hydraulic conductivity slightly decreases while the importance of sea-level rise and hydraulic gradient increases. As indicated by the upward pointing triangles, values above the susceptibility thresholds of hydraulic conductivity, and sea-level rise indicate susceptibility to climate-driven saline groundwater intrusion (Figure. 3). Meanwhile, the downward pointing triangles of hydraulic gradient and topographic gradient indicate susceptibility towards climate-driven saline groundwater intrusion for feature values below their susceptibility thresholds.

Figure 3 shows that, in 2000, hydraulic conductivities above 1.62 m/day tend to make aquifers susceptible to climate-driven saline groundwater intrusion. As climate change progresses, this susceptibility threshold declines, reaching 0.39 m/day by 2300. The shift in susceptibility threshold is likely induced by changing hydraulic gradients at the coast resulting from rising sea levels.

As climate-change progresses, the susceptibility threshold of sea-level rise increases from 0.04 m (2000) to 0.34 m (2300). Between 2000 and 2100, the susceptibility threshold of hydraulic gradient turns negative and reaches its minimum in 2200 at -0.00016. This shift is likely owed to the general increase in sea levels around the globe, changing the coastal hydraulic gradients. Thus, around the year 2100, a landward coastal hydraulic gradient is common where climate-driven saline groundwater intrusion occurs. From 2100 to 2200, the susceptibility threshold of topographic gradient decreases from 0.00284 (2100) to 0.00242 (2200) and then rises to 0.00267 (in 2300).

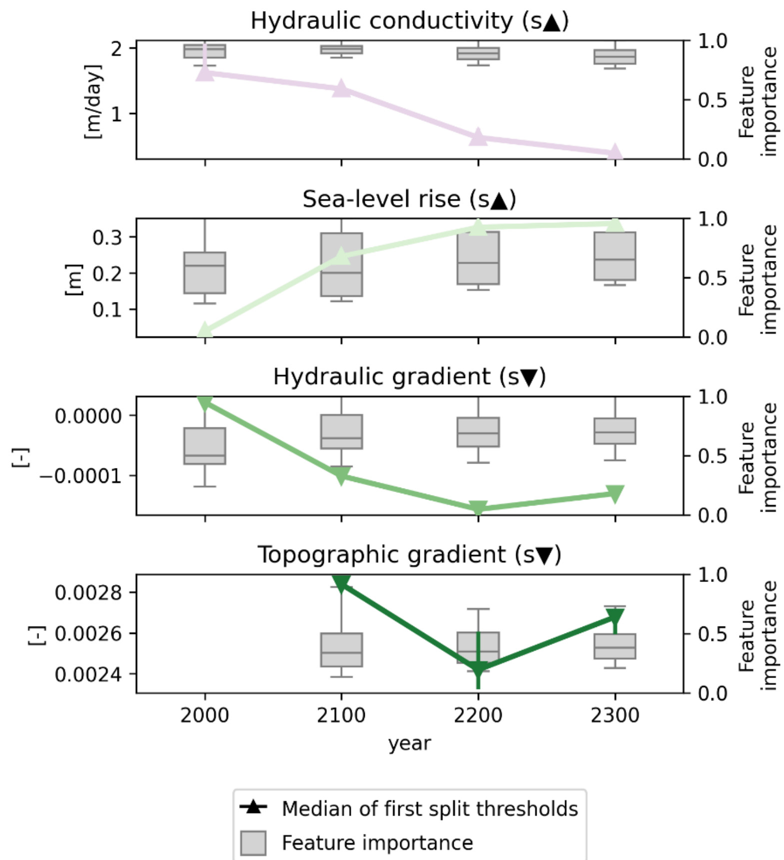

Figure 3 – Feature importance and susceptibility thresholds resulting from the random forest algorithm using change in salinity level by 2000, 2100, 2200, and 2300 as signal. Boxes show the feature importance of the model features hydraulic conductivity, sea-level rise, hydraulic gradient and topographic gradient. Colored lines show the susceptibility thresholds (i.e., medians of the random forest's first split). Triangles pointing up/down indicate that above/below the susceptibility threshold, groundwater was found to be mainly saline. Model cells with no change in salinity level are omitted in the evaluation. Groundwater recharge change is the main feature in no tree and aquifer thickness is only identified as a dominant feature in the year 2000. Therefore, groundwater recharge change and aquifer thickness are not shown in Figure 3 (for aquifer thickness results, see Figure S14). Model cells with no change in salinity level are omitted in the evaluation.

Using the thresholds delineated by the random forest algorithm, we analyze the area susceptible to saline groundwater intrusion due to physical factors. From 2000 to 2300, the largest area is susceptible due to sea-level rise, followed by hydraulic conductivity, hydraulic gradient and then topographic gradient (see Table S2). From 2000 to 2100, the global area susceptible to saline groundwater intrusion due to the evaluated factors increases from 2.67 to 3.06 million km^2, and remains stable thereafter (see Figure S16 to S18, and Table S2). This is a result of the large increase in area susceptible due to sea-level rise from 2000 to 2100 (2.27 to 2.91 km^2), remaining stable after 2100.

Figure 4 shows, for each climate reference region, the coastal area (i.e., < 100 km inland and < 100)[33] in which **a)** hydraulic conductivity, **b)** sea-level rise are above the respective threshold of the year 2300, and the area in which **c)** hydraulic gradient, **d)** topographic gradient are below their thresholds of the year 2300. As shown in Figure 4, in most climate regions an area of more than

10,000 km^2 is susceptible to saline groundwater intrusion due to sea-level rise. Meanwhile, in an area of less than 10,000 km^2 is susceptible due to the topographic gradient most climate regions.

While a larger area is susceptible to intrusion due to sea-level rise, hydraulic conductivity is identified as the most important feature by the random forest algorithm. Accordingly, Figure 1 shows low saline groundwater intrusion in 2300 (< 1 km^3) in those five climate regions where the area susceptible due to hydraulic conductivity is lower than 10,000 km^2 (see Figure 4). All five climate regions with high saline groundwater intrusion (> 5 km^3) have susceptible areas of more than 10,000 km^2 due to hydraulic conductivity, sea-level rise, hydraulic gradient and topographic gradient. In South East Asia (SEA), the climate region with the highest saline groundwater intrusion, the susceptible area is larger than 100,000 km^2 due to both hydraulic conductivity, sea-level rise, and hydraulic gradient. East North America (ENA) is the only climate region with a susceptible area above 100,000 km^2 (due to sea-level rise) but low saline groundwater intrusion (< 1 km^3).

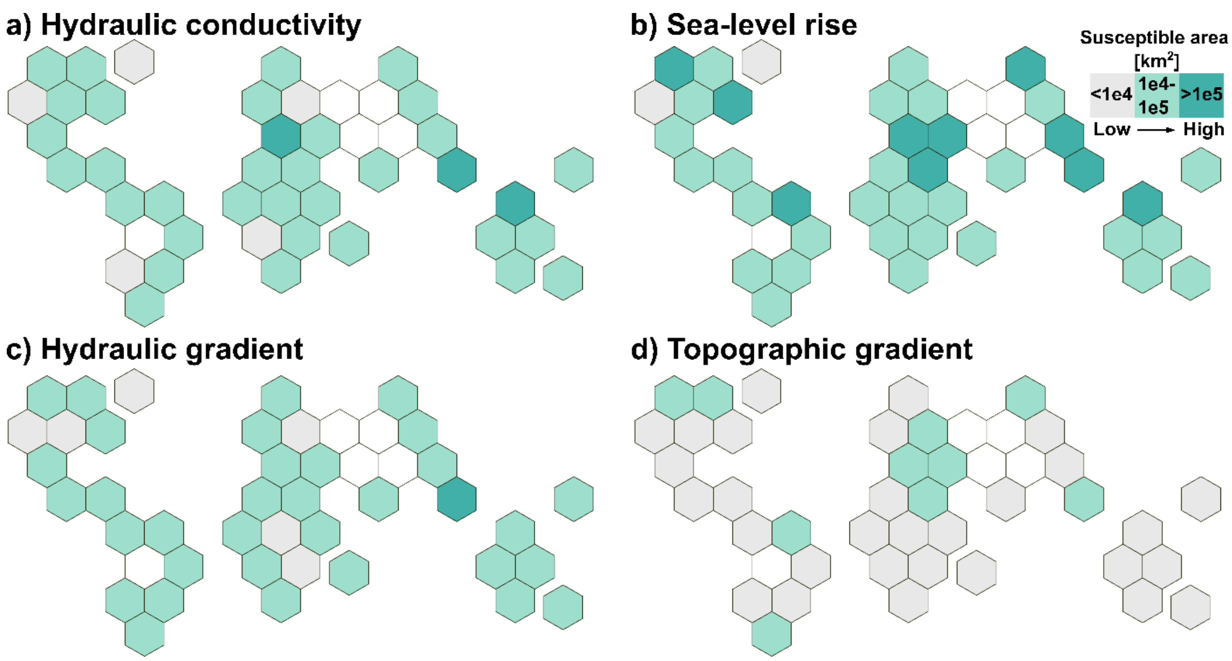

Figure 4 – Coastal area (i.e., < 100 km inland and < 100 m)[33] susceptible to saline groundwater intrusion due to physical factors in climate reference regions in 2300. White regions are landlocked. Colors show the coastal area within the climate reference regions, in which **a)** hydraulic conductivity, **b)** sea-level rise are above, and **c)** hydraulic gradient, **d)** topographic gradient are below their thresholds. Cells that cannot be reached by saline groundwater (i.e., with effective porosity equal 0 or cell elevation larger than or equal to aquifer thickness) are omitted in the evaluation. Hexagons adapted from ref. [22].

Discussion

Our findings indicate that when groundwater abstractions are accounted for, the risk to regions like the Mediterranean is imminent and substantial, while other regions globally may be more resilient to saline intrusion than previously assumed. Notably, we estimate that saline intrusion will affect 67% of the global coastline by 2100, a figure slightly lower than the recent estimate of 77% for coastal areas below 60° North[34]. Our model builds on previous work by incorporating development of inland gradients and surface water interactions and incorporating an ensemble of recharge projections. Further, we simulate a global saline groundwater intrusion volume of 108 km^3 by the year 2300 because of climate change. Since the prior simulation of an equilibrium state of coastal saline groundwater likely overestimates the initial volume of coastal saline groundwater, this additional volume is relatively modest compared to projected saline groundwater intrusion of 0.2 to 2.75 km^3 in the Netherlands alone by 2100[35].

We additionally find that more extensive saline groundwater intrusion is simulated in regions with higher hydraulic conductivity and sea-level rise. Most productive aquifers consist of highly conductive geologic units that will be particularly susceptible to intrusion. In contrast, higher hydraulic and topographic gradients can limit saline groundwater intrusion[25]. Notably, we find that the combination of these natural factors coupled with human variables yields substantial intrusion threats for several regions such as the Mediterranean, South Asia, and East Asia given their high dependence on groundwater and large populations at risk. Consequently, even modest increases in sea level and/or climate change may severely compromise freshwater availability for coastal communities, highlighting a time-sensitive need for adaptive water management strategies in vulnerable regions ranging from enhanced monitoring efforts, increases in water use efficiency, or development of alternative water sources.

Our conclusions, while accounting for many uncertainties, are limited by model and data constraints, yet they offer the most robust estimates of saline groundwater intrusion at the global scale to date. While our simulations of climate-driven saline groundwater intrusion do not include groundwater abstraction because future global pumping scenarios are not available, we incorporate present-day net abstraction estimates to calculate the potential risk. Another complicating factor is that groundwater recharge estimates are uncertain[36], and we thus use an ensemble estimate. To benchmark model performance, we previously quantified the similarities between model results and coastal groundwater salinity observations[26]. Another limitation of our approach is the lack of precise information on the structure and geometry of coastal aquifers globally. In our simulations, the deepest boundary of an aquifer can be above sea level (i.e., at high elevations and low aquifer thickness, see Figure S2d), creating a ledge over which intrusion cannot occur. Therefore, no intrusion is possible in 31.3% of the simulated coastline in the initial long-term equilibrium simulation, and 30.2% in 2300. Our focus on only the shallowest aquifer leads to an underestimation of climate-driven saline groundwater intrusion that would occur into deeper aquifers not included in our model framework. Thus, our results are valid only for the shallowest coastal aquifers, where deeper aquifers would require additional geologic controls to simulate (see also Text S2,3 regarding the model sensitivity analysis and model assumptions).

Using an equilibrium state as initial condition and extending almost 300 years into the future, we show that even moderate sea-level rise poses a significant threat to coastal aquifers and those who rely on their water resources. We expect that the risk of saline groundwater intrusion is underestimated (i.e., conservative from a threat perspective), particularly given our use of present-day populations relative to the projected increase in global coastal populations. For example, coastal populations are expected to grow from 54 million to 245 million in Africa and 461 million to 983 million in Asia by 2060, a 4.5-fold and 2.1-fold increase, respectively[11]. Our findings indicate that saltwater may reach far inland, revealing a risk that has not been fully recognized thus far. The finding suggests that the potential for saline groundwater intrusion could be much greater than previously thought, highlighting future challenges to coastal water resources even without increasing demand. However, if population growth continues without implementing alternative water management programs, we can expect groundwater extraction to remain stable or increase, likely worsening the problem of saline groundwater intrusion. As groundwater salinizes, societies may be forced to transport water from inland sources to coastal areas while at the same time facing negative impacts on municipal infrastructure[37,38], or, in scenarios where this is impractical, face limitations on rapid population growth or emigration in these regions. These findings underscore the time-sensitive need for policymakers to prioritize sustainable water management strategies in coastal areas[39] to mitigate the potential impacts of climate change and population growth and support further study[40] of the pathways of and feedbacks between water resources, climate change, and human activities.

Methods

Modeling global variable density groundwater

To simulate global saltwater intrusion, we have developed the Global Gradient-based Groundwater Model with variable Densities (G^3M-D)[26,41,42]. G^3M-D simulates sharp interfaces which separate groundwater into vertically stacked salinity zones (i.e., here, fresh and saline water)[26]. The height of these density interfaces changes when the proportions of salinity zones change within model cells. While more details, including model mechanisms, are given in Text S1, the applied equations and subroutines are described in ref. [26,43].

We employ three simulation phases to model variable density in global coastal groundwater (see Figure S3). Starting from a system with entirely fresh groundwater, (1) a long-term equilibrium simulation is run with a 1000-year time step for groundwater heads, while updating the freshwater-saltwater interface annually. This phase uses the steady mean groundwater recharge and sea level from the 1861–1890 ISIMIP ensemble, running until the sharp interface stabilized after approximately 485,000 years. Using the stabilized interface heights as inputs, (2) a transient simulation with a 1-year time step is run, representing the 1891-2300 period. The transient simulation isolates climate-related effects on saline groundwater intrusion by incorporating annually changing groundwater recharge (based on an ensemble mean of eight global hydrological models) and relative sea level rise[28,29] from 1891 to 2300 (Figures S10-S13). The applied sea-level rise projections represent the socioeconomic path RCP 2.6 (i.e., very low emissions pathway), which is preferred over other pathways since it is the only extended projection (until 2300). Groundwater extractions, which are driving large parts of saline groundwater intrusion, are not included in the transient simulation, since they are highly uncertain and no global gridded datasets are available to parameterize the model. Additionally, (3) an equilibrium extension simulation is run, which maintains constant mean groundwater recharge and sea level from the 1861–1890 baseline throughout the 1891–2300 period, and is subtracted from the transient simulation to remove artifacts of the residual salinization occurring after 485,000 years of the long-term equilibrium simulation.

Risk, the combination of hazard, exposure and vulnerability, is changing

The hazard, vulnerability, exposure framework is a structured way to assess risk by looking at the relationship between harmful events (hazard), the places or people exposed to them (exposure), and the susceptibility to be harmed (vulnerability). In this framework, risk is the combination (product of normalized values) of hazard, exposure, and vulnerability[44]. Here, we use the

1) volume of saline groundwater intrusion (= saltwater interface rise * effective porosity * area) as **hazard**,

2) population count in 2020[31] as **exposure,** and

3) volume of net groundwater abstraction[27] as **vulnerability.**

Risk is defined here as the product calculated by multiplying the normed hazard, exposure and vulnerability (i.e., risk = hazard' * exposure' * vulnerability'). We applied the Min-Max Normalization method:

$$x' = \frac{x - x_{min}}{x_{max} - x_{min}}$$

Due to high uncertainties in future social scenarios, and to highlight the future impact of saline groundwater intrusion, exposure, and vulnerability are held constant at present values. While freshening occurs in northern climate reference regions with temporarily declining relative sea levels, our evaluations focus on saline groundwater intrusion.

Since no suitable global dataset of fresh groundwater abstraction exists, we do not include freshwater sources themselves but use simulated net groundwater abstraction data from ref. [27] as vulnerability. Only model cells with changing saltwater content were included in the evaluations. Thus, exposure (population) and vulnerability (net groundwater abstraction) have been assessed only in cells with changing saltwater content.

Using sensitivity analysis to assess which features drive intrusion

The random forest algorithm, an ensemble machine learning method, was run with 1000 decision trees, using the Gini coefficient as measure of impurity, to rank the assessed features by their feature importance. Further, we extract the root split threshold of all decision trees to understand which feature ranges make coastal aquifers prone to saline groundwater intrusion. Evaluating at multiple time steps, we find how the root split thresholds change over time. We calculate the threshold (i.e., the threshold above/below which saline groundwater intrusion can be expected) as the median the of root split thresholds in the random forest trees.

The assessed hydro(geo)logical features are: aquifer depth (D_{aqu}), hydraulic conductivity (K), sea-level rise (SLR), groundwater recharge change (GWRC), hydraulic gradient (dH), and topographic gradient (dT). The analyzed signal is change in saline interface height. The evaluated years are 2000, 2100, 2200, and 2300, compared to 2025. GWRC is the main feature (i.e., the feature used in the first split) in no tree and D_{aqu} is only identified as a dominant feature in the year 2000. Model cells with no change in salinity level are omitted in the evaluation.

To test the plausibility of the random forest algorithm outcome, we use the PAWN method, a global, non-parametric sensitivity analysis technique[45], to rank the input variables by their control over model outputs. A short explanation of random forest and PAWN is given in Text S3. The rankings derived from the results of the random forest algorithm and the PAWN method are consistent (see Figure S15). While PAWN confirms that GWRC is the factor with the least control over the change in salinity level, GWRC is not entirely irrelevant.

Data availability statement

The data that support the findings of this study are available online, separated into a dataset with constant data and one with time-variant data.

The dataset with constant data contains model inputs (i.e., area of cells, aquifer depth, effective porosities and hydraulic conductivities), as well as data used for evaluation (i.e., annual net abstraction from groundwater, and population count, identifier of climate reference regions). The dataset with time-variant data contains the model input relative sea level rise, and the model outputs difference in saline groundwater interface height compared to the year 2025, hydraulic gradients, topographic gradients and climate-driven saline groundwater intrusion for the years 2100, 2200, 2300.

The link to the data repository is as follows: https://zenodo.org/records/18399014?preview=1&token=eyJhbGciOiJIUzUxMiJ9.eyJpZCI6IjNkNmQzNGU5LTVhMjItNGQyMy05OWM5LTJmYjAxMGRhMGY0OCIsImRhdGEiOnt9LCJyYW5kb20iOiI3ZjlkMWE2YWQyZmU1MjQ1OTU2MDQ2OTJhODNkMGY4NiJ9.SKGoRaoPWKH0BOZJXoEyLVGwLHIPmVxIyBoOoJx0QvunO26BDBq8rESQ6omNmn-5eHNK_a4NzVAIJl20GsKdXA

Acknowledgements

D K is funded by Deutsche Forschungsgemeinschaft (G Z: RE 4624/1-1). T W was funded by the Alexander von Humboldt Foundation in the framework of the Alexander von Humboldt Professorship endowed by the German Federal Ministry of Education and Research. HM acknowledges support from the US National Science Foundation EPSCoR (2446056) and Critical Zone Network (EAR2012484) programs. M B was funded by the ERC Advanced Grant Scheme (project GEOWAT No. 101019185).

References

1. Center for International Earth Science Information Network (CIESIN). National Aggregates of Geospatial Data: Population, Landscape and Climate Estimates Version 3 (PLACE III). Earthdata https://doi.org/10.7927/H4F769GP (2012).

2. Johnson, T. D., Belitz, K., Kauffman, L. J., Watson, E. & Wilson, J. T. Populations using public-supply groundwater in the conterminous U.S. *Science of the Total Environment* **806**, 150618 (2022).

3. Morris, B. L., Lawrence, A. R. L., Chilton, P. J. C., Adams, B., Calow, C. R. & Klinck, B. A. *Groundwater and its susceptibility to degradation* (United Nations Environment Programme, 2003).

4. White, I. & Falkland, T. Management of freshwater lenses on small Pacific islands. *Hydrogeology Journal* **18**, 227–246 (2010).

5. Huang, Z., Hejazi, H., Li, X., Tang, Q., Vernon, C., Leng, G., Liu, Y., Döll, P., Eisner, S., Gerten, D., Hanasaki, N. & Wada, Y. Reconstruction of global gridded monthly sectoral water withdrawals for 1971–2010. *Hydrology and Earth System Sciences* **22**, 2117–2133 (2018).

6. Jasechko, S., Seybold, H., Perrone, D., Fan, Y., Shamsudduha, M., Taylor, R. G., Fallatah, O. & Kirchner, J. W. Rapid groundwater decline and some cases of recovery in aquifers globally. *Nature* **625**, 715–721 (2024).

7. Oppenheimer, M., Glavovic, B. C., Hinkel, J., van de Wal, R., Magnan, A. K., Abd-Elgawad, A., Cai, R., Cifuentes-Jara, M., DeConto, R. M., Ghosh, T., Hay, J., Isla, F., Marzeion, B., Meyssignac, B. & Sebesvari, Z. Sea level rise and implications for low-lying islands, coasts and communities. In *IPCC Special Report on the Ocean and Cryosphere*, 321–445 (Cambridge University Press, 2019).

8. Taylor, R. G., Scanlon, B., Döll, P., Rodell, M., van Beek, R., Wada, Y., Longuevergne, L., Leblanc, M., Famiglietti, J. S., Edmunds, M., Konikow, L., Green, T. R., Chen, J., Taniguchi, M., Bierkens, M. F. P., MacDonald, A., Fan, Y., Maxwell, R. M., Yechieli, Y., Gurdak, J. J., Allen, D. M., Shamsudduha, M., Hiscock, K., Yeh, P. J.-F., Holman, I. & Treidel, H. Ground water and climate change. *Nature Climate Change* **3**, 322-329 (2013).

9. Zamrsky, D., Oude Essink, G. H. P. & Bierkens, M. F. P. Global impact of sea level rise on coastal fresh groundwater resources. *Earth's Future* **12** (2024).

10. Berghuijs, W. R., Collenteur, R. A., Jasechko, S., Jaramillo, F., Luijendijk, E., Moeck, C., van der Velde, Y. & Allen, S. T. Groundwater recharge is sensitive to changing long-term aridity. *Nature Climate Change* **14**, 357–363 (2024).

11. Neumann, B., Vafeidis, A. T., Zimmermann, J. & Nicholls, R. J. Future coastal population growth and exposure to sea-level rise. *PLOS ONE* **10**, e0118571 (2015).

12. Barlow, P. M. & Reichard, E. G. Saline groundwater intrusion in coastal regions of North America. *Hydrogeology Journal* **18**, 247–260 (2010).

13. Custodio, E. Coastal aquifers of Europe: an overview. *Hydrogeology Journal* **18**, 269–280 (2010).

14. Prusty, P. & Farooq, S. H. Seawater intrusion in the coastal aquifers of India – A review. *HydroResearch* **3**, 61–74 (2020).

15. Perera, M. D. N. D., Ranasinghe, T. K. G. P., Piyadasa, R. U. K. & Jayasinghe, G. Y. Risk of seawater intrusion on coastal community of Bentota river basin Sri Lanka. *Procedia Engineering* **212**, 699–706 (2018).

16. Ghirardelli, A., Straffelini, E., Park, E., D'Agostino, V., Masin, R. & Tarolli, P. Global impact of seawater intrusion on coastal agriculture. *Environmental Research Letters* **20**, 1 (2025).

17. Cooper, H. H. Jr., Kohout, F. A., Henry, H. R. & Glover, R. E. Sea water in coastal aquifers. *U.S. Geological Survey Water-Supply Paper* **1613-C** (1964).

18. Werner, A. & Simmons, C. T. Impact of sea-level rise on sea water intrusion in coastal aquifers. *Ground Water* **47**, 197–204 (2009).

19. Thorslund, J., Bierkens, M. F. P., Oude Essink, G. H. P., Sutanudjaja, E. H. & van Vliet, M. T. H. Common irrigation drivers of freshwater salinisation. *Nature Communications* **12**, 4232 (2021).

20. Werner, A. D., Bakker, M., Post, V. E. A., Vandenbohede, A., Lu, C., Ataie-Ashtiani, B., Simmons, C. T. & Barry, D. A. Seawater intrusion processes, investigation and management. *Advances in Water Resources* **51**, 3–26 (2013).

21. Cao, T., Han, D. & Song, X. Past, present, and future of global seawater intrusion research: A bibliometric analysis. *Journal of Hydrology* **603**, 126844 (2021).

22. IPCC. Summary for Policymakers. In *Climate Change 2021: The Physical Science Basis*, 3–32 (Cambridge University Press, 2021).

23. Richardson, C. M., Davis, K. L., Ruiz-González, C., Guimond, J. A., Michael, H. A., Paldor, A., Moosdorf, N. & Paytan, A. The impacts of climate change on coastal groundwater. *Nature Reviews Earth & Environment* **5**, 100–119 (2024).

24. Befus, K. M., Barnard, P. L., Hoover, D. J., Finzi Hart, J. A. & Voss, C. I. Increasing threat of coastal groundwater hazards from sea-level rise in California. *Nature Climate Change* **10**, 946–952 (2020).

25. Michael, H. A., Russoniello, C. J. & Byron, L. A. Global assessment of vulnerability to sea-level rise in coastal groundwater systems. *Water Resources Research* **49**, 2228–2240 (2013).

26. Kretschmer, D. V., Michael, H. A., Moosdorf, N., Oude Essink, G. H. P., Bierkens, M. F. P., Wagener, T. & Reinecke, R. Controls on coastal saline groundwater across North America. *Environmental Research Letters* **20**, 024065 (2025).

27. Müller-Schmied, H. *et al.* The global water resources and use model WaterGAP v2.2d. PANGAEA https://doi.org/10.1594/PANGAEA.918447 (2020).

28. Mengel, M., Levermann, A., Frieler, K., Robinson, A., Marzeion, B. & Winkelmann, R. Future sea level rise constrained by observations and long-term commitment. *Proceedings of the National Academy of Sciences USA* **113**, 2597–2602 (2016).

29. Mengel, M. ISIMIP2b sea-level rise input data (v1.0). ISIMIP Repository https://doi.org/10.48364/ISIMIP.768189 (2017).

30. Iturbide, M. *et al.* An update of IPCC climate reference regions for subcontinental analysis of climate model data. *Earth System Science Data* **12**, 2959–2970 (2020).

31. Center for International Earth Science Information Network (CIESIN). *Documentation for the Gridded Population of the World, Version 4 (GPWv4), Revision 11 Data Sets* (2018).

32. Wagener, T., Reinecke, R. & Pianosi, F. On the evaluation of climate change impact models. *WIREs Climate Change* **13**, e772 (2022).

33. Small, C. & Nicholls, R. J. A global analysis of human settlement in coastal zones. *Journal of Coastal Research* **19**, 584–599 (2003).

34. Adams, K. H., Reager, J. T., Buzzanga, B. A., David, C. H., Sawyer, A. H. & Hamlington, B. D. Climate-induced saltwater intrusion in 2100: Recharge-driven severity, sea level-driven prevalence. *Geophysical Research Letters* **51**, e2024GL110359 (2024).

35. Oude Essink, G. H. P., van Baaren, E. S. & De Louw, P. G. B. Effects of climate change on coastal groundwater systems. *Water Resources Research* **46** (2010).

36. Reinecke, R., Müller Schmied, H., Trautmann, T., Andersen, L. S., Burek, P., Flörke, M., Gosling, S. N., Grillakis, M., Hanasaki, N., Koutroulis, A., Pokhrel, Y., Thiery, W., Wada, Y., Yusuke, S. & Döll, P. Uncertainty of simulated groundwater recharge at different global warming levels: a global-scale multi-model ensemble study. *Hydrology and Earth System Sciences* **25,** 787-810 (2021).

37. Habel, S., Fletcher, C. H., Barbee, M. M. & Fornace, K. L. Hidden threat: The influence of sea-level rise on coastal groundwater and the convergence of impacts on municipal infrastructure. *Annual Review of Marine Science* **16** (2024).

38. Kurylyk, B. L., Russoniello, C. J., Guimond, J. A., Habel, S., Michael, H. A., Sukop, M. C. & Wilson, A. M. Invisible groundwater threats to coastal urban infrastructure. *Nature Cities* **2**, 775–777 (2025).

39. Michael, H. A., Post, V. E. A., Wilson, A. M. & Werner, A. D. Science, society, and the coastal groundwater squeeze. *Water Resources Research* **54**, 2610–2617 (2017).

40. Helton, A. M., Dennedy-Frank, P. J., Emanuel, R. E., Neubauer, S. C., Adams, K. H., Ardon, M., Band, L., Befus, K. M., Borstlap, H., Duberstein, J. A., Gold, A. C., Kominoski, J. S., Manda, A. K., Michael, H. A., Moysey, S. M. J., Myers-Pigg, A. N., Neville, J. A., Noe, G., Panthi, J., Pezeshki, E., Sirianni, M. J. & Ward, N. D. Over, under, and through: Hydrologic connectivity and the future of coastal landscape salinization. *Water Resources Research* **61**, e2024WR038720 (2025).

41. Reinecke, R., Foglia, L., Mehl, S., Herman, J. D., Wachholz, A., Trautmann, T. & Döll, P. Spatially distributed sensitivity of simulated global groundwater heads and flows. *Hydrology and Earth System Sciences* **23**, 4561–4582 (2019).

42. Reinecke, R., Foglia, L., Mehl, S., Trautmann, T., Cáceres, D. & Döll, P. Challenges in developing a global gradient-based groundwater model. *Geoscientific Model Development* **12**, 2401–2418 (2019).

43. Bakker, M., Schaars, F., Hughes, J. D., Langevin, C. D. & Dausman, A. M. Documentation of the Seawater Intrusion (SWI2) Package for MODFLOW. *U.S. Geological Survey Techniques and Methods* **6**, chap. A46 (2013).

44. Cardona, O. D., van Aalst, M. K., Birkmann, J., Fordham, M., McGregor, G., Perez, R., Pulwarty, R. S., Schipper, E. L. F. & Sinh, B. T. Determinants of risk: exposure and vulnerability. In *Managing the Risks of Extreme Events and Disasters to Advance Climate Change Adaptation*, 65–108 (Cambridge University Press, 2012).

45. Pianosi, F. & Wagener, T. Distribution-based sensitivity analysis from a generic input-output sample. *Environmental Modelling & Software* **108**, 197–207 (2018).

Supplement of

Two-thirds of global coastline affected by climate-driven saline groundwater intrusion by end of century, reaching far inland by 2300

Kretschmer et al.

Corresponding author: Daniel V. Kretschmer (dkretsch@uni-mainz.de)

Contents of this file

Text S1 to S6

Figures S1 to S18

Table S1 to S2

Introduction

The supporting information is presented following the outline of the main text.

Text S1 – The global gradient-based groundwater model

The global gradient-based groundwater model, G^{3}M[1,2], was developed based on concepts of MODFLOW-2005[3] and designed for coupling with global hydrological models. In G^{3}M, three-dimensional groundwater flow is driven by hydraulic gradients between grid cells. The respective partial differential equation is defined as follows[3]:

$$\frac{\partial}{\partial x}\left(K_{xx}\frac{\partial h}{\partial x}\right)+\frac{\partial}{\partial y}\left(K_{yy}\frac{\partial h}{\partial y}\right)+\frac{\partial}{\partial z}\left(K_{zz}\frac{\partial h}{\partial z}\right)+W=S_s\frac{\partial h}{\partial t}$$

where K_{xx}, K_{yy}, and K_{zz} [LT^{-1}] are the hydraulic conductivities along the axes (x, y, and z) between grid cells with lengths Δx, Δy, and Δz [L]; S_s [L^{-1}] is the specific storage; h [L] is the hydraulic head. W [T^{-1}] represents sources and sinks of each cell, including groundwater recharge and interaction with surface water (rivers, lakes, wetlands, ocean). Similar to the flows between the model cells, the flow of groundwater from a cell to surface water depends on the heads. Cells may therefore receive/give water from/to surrounding cells and additionally from/to surface waters (rivers, lakes, wetlands, ocean).

The variable density routine

We have implemented a model routine for G^{3}M that takes variable groundwater densities into account. In the new model, Global Gradient-based Groundwater Model with variable Densities (G^{3}M-D), sharp interfaces separate different salinity zones. The interface height is simulated using a routine similar to the Saltwater Intrusion package (SWI2) for MODFLOW[4] – chosen for its low computational demand – essential for global-scale modeling. Compared to G^{3}M, simulating groundwater heads only, G^{3}M-D adds a variable density routine. The head calculations account for the density zone volumes before solving the variable density flow. When simulating variable densities, the mass balance equation of G^{3}M is replaced by a volume balance equation[4]. In this volume balance equation, effective porosity is used to scale the density interface height changes. To accelerate interface movement, multiple shorter variable density time steps can be simulated within each groundwater flow step.

Density zones and density interfaces

Freshwater is less dense than saline water. In G^{3}M-D, like in SWI2, density zones vertically stacked in each cell (see Figure S1). The model simulates the height of sharp horizontal interfaces separating zones of constant density (i.e., this corresponds to the discontinuous option in SWI2). In this study, one interface separates freshwater and saltwater zones, approximating the 50% saltwater salinity boundary. Density interface height changes occur when proportions of saline zones change. At each density time step, interface heights are iteratively computed for all cells containing saline water. Interface adjustments then account for horizontal movement of saline water from a cell containing saline water to intrude neighboring freshwater cells when the slope between the interface and the bottom of the freshwater cell is above a threshold. For equations and subroutines of the density routine, see ref. [4,5].

Model mechanisms

In G^{3}M-D, freshwater inputs (from groundwater recharge, rivers, or neighboring cells) raise groundwater heads, while inflows of saline groundwater (from the ocean or neighboring cells) can elevate the density interface. At the coast, several model mechanisms control the distribution of salinity (Figure S2). Similar to the Badon Ghijben-Herzberg relation, higher freshwater heads can force saline water out of a cell, lowering the density interface. Consequently, steep terrain (high dT) can limit salinization if freshwater heads are high (i.e., if hydraulic conductivity is low and/or groundwater recharge is high) (Figure S2 a) and b)). If aquifer depth (i.e., depth to bedrock) remains shallow inland, steep terrain can position cell bottoms above neighboring saline zones, restricting lateral salinization. In contrast, flat terrain (low dT) allows saline water to penetrate farther inland (Figure S2 a) and b)). Figure S2 c) and d) show that low aquifer depth, paired with low cell top elevation may prohibit salinization by disconnecting the cell from the ocean. In contrast, salinization of cells with high top elevation can occur if the aquifer depth is high (Figure 2 e) and f)). Cells with low groundwater recharge have lower freshwater heads, reducing the freshwater column and allowing deeper intrusion (Figure S2 f) and g)). High hydraulic conductivity promotes larger drainage rates (i.e., to neighboring cells, rivers or the ocean), and lower fresh groundwater levels, increasing the potential for saltwater intrusion (Figure S2 h) and i)).

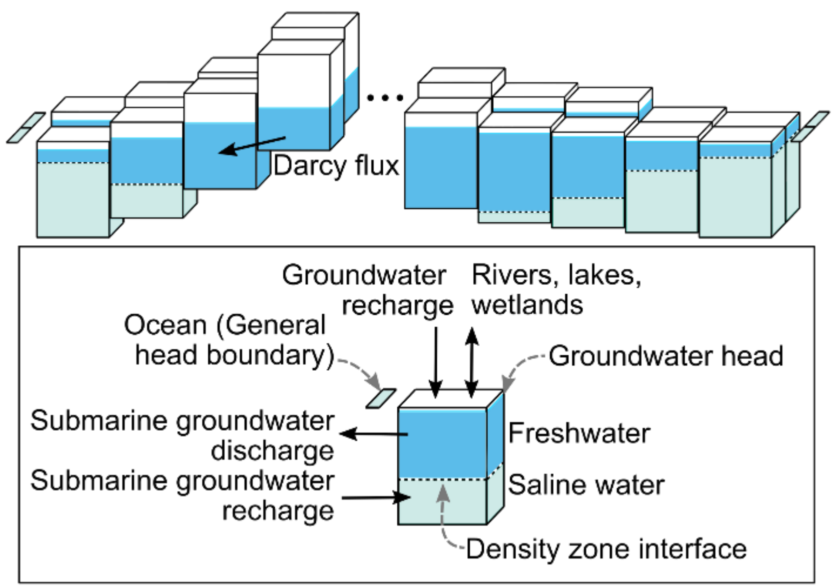

Figure S1 – The concept of the variable density groundwater model (G^3M-D).

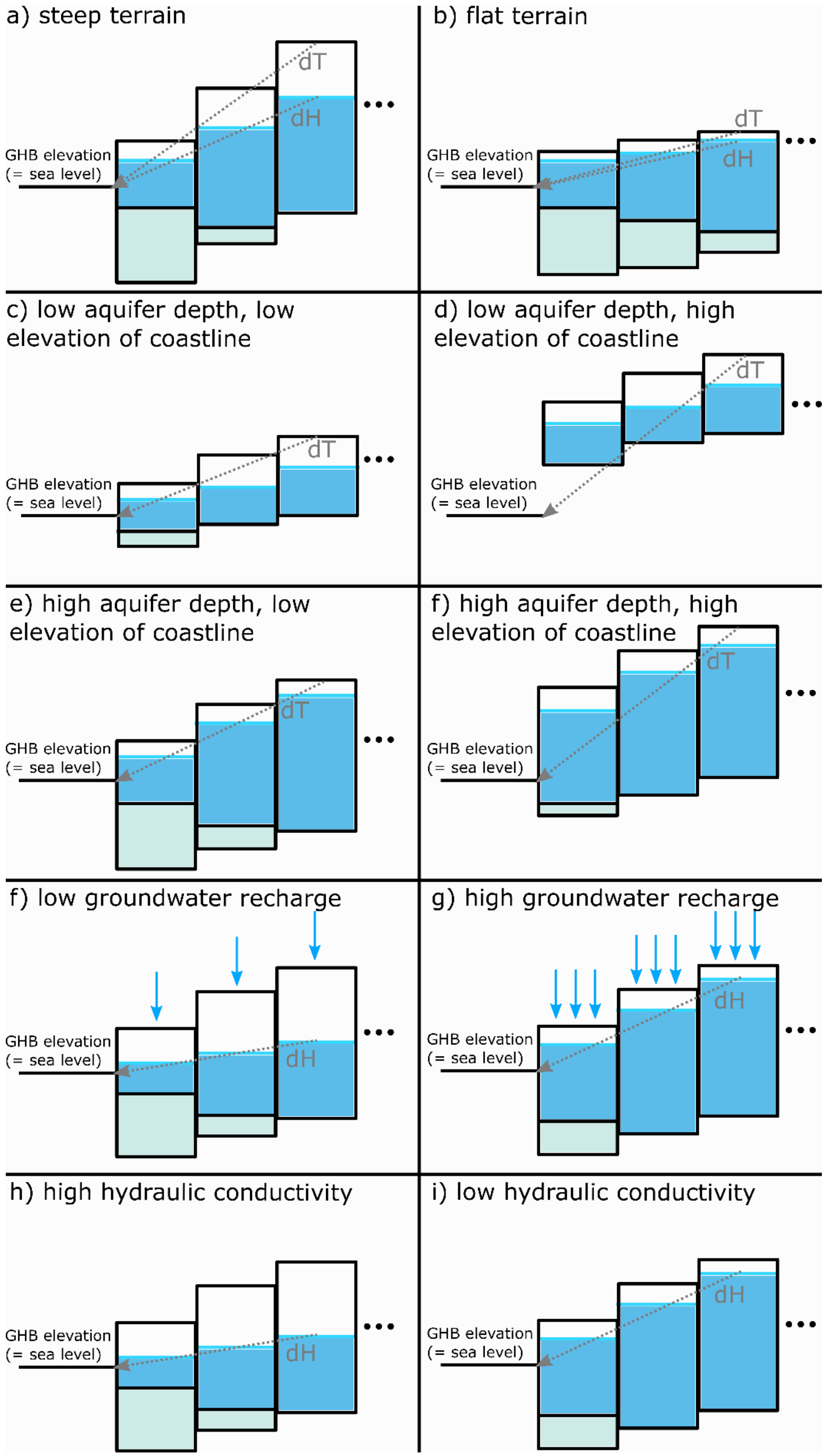

Figure S2 – Conceptual figure of model mechanisms in G³M-D.

Text S2 - Model limitations and assumptions

The variable density routine in G³M-D relies on four key approximations (see ref. [4]): (1) vertical flow resistance within aquifers is neglected (Dupuit approximation); (2) a volume balance equation is used for flow calculations (Boussinesq-Oberbeck approximation); (3) dispersion and diffusion are considered negligible; and (4) density inversions are only allowed between, not within, aquifers. These assumptions reduce computational demands and enable global coastal groundwater density simulation.

Furthermore, the spatial resolution of 5 arcmin is coarse for the simulation of saline groundwater. While many important coastal features (e.g., mangroves, cliffs, beaches) cannot be represented at a scale of 5 arcmin, we lack global datasets containing detailed information (e.g., permeabilities at different depths, and related aquifer depths) that would justify simulations using a higher resolution. The implemented sharp horizontal interface (a consequence of the underlying approximations) can cause saline groundwater entering one side of a cell to raise the interface, allowing rapid lateral movement into neighboring cells in subsequent time steps — potentially transporting salinity over several kilometers per year. This likely overestimates the velocity of saline groundwater movement compared generally slower to real-world hydrodynamic dispersive processes. Despite this, the model required 485,000 years to reach an equilibrium state under steady climatic forcing (i.e. sea level and groundwater recharge mean for 1861 to 1890), suggesting global saline groundwater patterns have been evolving since before the last glacial maximum (~20,000 years ago). The model excludes anthropogenic impacts (e.g., pumping), and omits inland salinity sources.

The projections of climate-driven saline groundwater intrusion likely underestimate the actual extent for several reasons. Due to a lack of global data on current coastal groundwater salinity, the initial condition of the transient simulation was set using a long-term equilibrium simulation representing climatic forcing from 1861 to 1890 (simulated 485,000 years). Therefore, the transient simulation only tracks the saline groundwater intrusion added by anthropogenic climate change, and does not include ongoing intrusion originating from climatic oscillations since the last glacial period approximately 12,000 years ago. Also, in the applied climate change scenario (RCP2.6), the mean sea-level rise projected for 2300 is 0.87 m, which is at the lower end of sea-level rise projections[6].

Text S3 – Model input, feature uncertainties and simulations

Model input

The G³M-D model setup uses several global datasets. The parameterization of elevation and surface water bodies (rivers, lakes, wetlands) follows ref. [1,2]. Hydraulic conductivity and effective porosity are taken from GLHYMPS 2.0[7], with mean values of 8.45 m/day and 0.05, respectively. Specific storage was set to 0.000015, following ref. [8]. Cells with zero effective porosity (48.7% overall, 23.6% along the coast) are excluded from the variable density routine. Karstic and volcanic conduits are not represented. Similar to the groundwater simulations by ref. [8], groundwater recharge is based on an ensemble of eight global hydrological models retrieved from the ISIMIP database (https://www.isimip.org/), with a mean of 0.28 mm/day[9]. Aquifer thickness is defined using depth to bedrock data (mean: 31.78 m)[10], with no aquitards or deep confined layers represented. Ocean boundaries are modeled using a general head boundary (GHB)[3] with a coastal shoreline permeability of the CoPerm dataset[11], which was converted to hydraulic conductivity (K = k*rho*g/mu) using a density of rho=999.97 kg/m^3, and viscosity of seawater mu=0.001 kg/m s and an acceleration due to gravity of g=9.8 m/s^2. Sea levels are parameterized using global projections to 2300[12,13]. These sea level projections use a historical socioeconomic pathway for the period 1861-2005, and Representative Concentration Pathway (RCP) 2.6 for the period 2006-2299. The model assumes the ocean is the sole saltwater source, omitting known inland salinity deposits[14,15]. Two density zones are simulated: freshwater (999.5 kg/m^3 at 0 ppt) and saltwater (1,026.6 kg/m^3 at 35 ppt), based on a constant groundwater temperature of 12°C.

Feature uncertainties

Global input datasets have substantial uncertainties. GLHYMPS permeability values are precise to roughly order of magnitude[1]. Permafrost transmissivity is simplified, based on low conductivity values without accounting for complexities such as ice layering. Depth to bedrock estimates are also highly uncertain[10]. Groundwater recharge estimates differ widely across datasets[8]. The model setup reflects a best-estimate parameterization, but will likely not reproduce or forecast salinity distributions to a precision needed for local groundwater resource management.

Simulation runs

First, the dynamic equilibrium fresh-saline groundwater interface position per cell was simulated in a long-term equilibrium simulation. At the beginning of this simulation, all groundwater in the model domain was fresh. Throughout the simulation, saline ocean water intruded via the general head boundary, which was set to the mean sea levels of 1861-1890[12,13]. As density changes occur much more slowly than groundwater heads, the simulation was run with pseudo-steady-state boundary conditions[4], with constant sea level, coastline, and recharge rates (mean of 1861-1890), while iteratively updating density interface positions. For each 1,000-year groundwater flow time step, 1,000 annual density time steps were simulated. The model was run until interface heights stabilized, defined by two consecutive 1,000-year steps in which (a) 95% of saline water cells showed interface changes < 0.05 m, and (b) 99% showed changes < 0.1 m. This stability criteria were only reached after 485,000 years.

A transient and equilibrium extension simulation, using the stable interface positions captured from the long-term dynamic equilibrium simulation, were run simulating the period from 1891 to 2300. While the equilibrium extension simulation is a continuation of the long-term equilibrium simulation, sea levels and groundwater recharge inputs change at every annual time step in the transient simulation. To make sure that the interface changes in the transient simulation are not artifacts of the ongoing but very slow salinization of global aquifers, any interface movement simulated in the equilibrium extension simulation was subtracted from the transient simulation results.

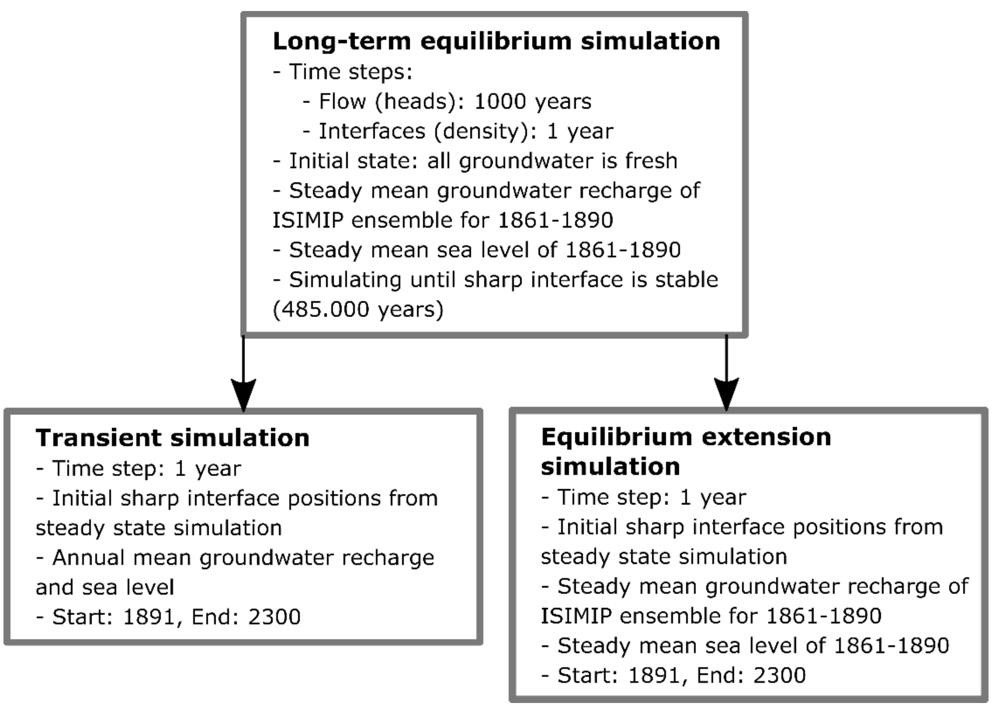

Figure S3 – Employed simulation runs.

Text S4 – Climate Reference Regions

The climate reference regions provide a framework for the robust assessment and inter-comparison of climate variability, trends, and projected changes[16]. The 46 ocean and 15 land regions were delineated based on climatological characteristics to enable consistent aggregation and interpretation of observational and model-derived data. Their application ensures comparability between studies, enhances the detection of regional climate signals, and supports the formulation of regionally targeted climate risk assessments and policy responses.

The hexagons displaying the climate reference regions were adapted from ref. [17]. In these hexagons, the climate reference regions EPO (Equatorial Pacific Ocean), SPA (South Pacific Ocean), and NPO (North Pacific Ocean) are combined into in one named PAC (Pacific Ocean). Further, the climate reference regions ARO (Arctic Ocean), ARS (Arabian Sea), and BOB (Bay of Bengal) are not shown.

Table S1 – List of abbreviations for climate reference regions[16]

Acronym	Name	Region	CRR ID
ARO	Arctic Ocean	ARCTIC	0
ARP	Arabian Peninsula	ASIA	1
ARS	Arabian Sea	INDIAN	2
BOB	Bay of Bengal	INDIAN	3
CAF	Central-Africa	AFRICA	4
CAR	Caribbean	CENTRAL-AMERICA	5
CAU	Central-Australia	OCEANIA	6
CNA	Central-North-America	NORTH-AMERICA	7
EAO	Equatorial Atlantic Ocean	ATLANTIC	8
EAS	East-Asia	ASIA	9
EAU	East-Australia	OCEANIA	10
ECA	East Central Asia	ASIA	11
EEU	East-Europe	EUROPE	12
EIO	Equatorial Indic Ocean	INDIAN	13
ENA	East North-America	NORTH-AMERICA	14
ESAF	East Southern-Africa	AFRICA	15
ESB	East-Siberia	ASIA	16
GIC	Greenland/Iceland	POLAR	17
MDG	Madagascar	AFRICA	18
MED	Mediterranean	EUROPE-AFRICA	19
NAO	North Atlantic Ocean	ATLANTIC	20
NAU	Northern Australia	OCEANIA	21
NCA	Northern Central-America	CENTRAL-AMERICA	22
NEAF	North-Eastern-Africa	AFRICA	23
NEN	North-Eastern North-America	NORTH-AMERICA	24
NES	North-Eastern South-America	SOUTH-AMERICA	25
NEU	North-Europe	EUROPE	26
NSA	Northern South-America	SOUTH-AMERICA	27
NWN	Northern West-North-America	NORTH-AMERICA	28
NWS	Southern Central-America	CENTRAL-AMERICA	29
NZ	New-Zealand	OCEANIA	30
PAC	Pacific Small Islands	OCEANIA	31
RAR	Russian-Arctic	ASIA	32
RFE	Russian-Far-East	ASIA	33
SAH	Sahara	AFRICA	34
SAM	South-American-Monsoon	SOUTH-AMERICA	35
SAS	South-Asia	ASIA	36
SAU	South-Australia	OCEANIA	37
SCA	South Central-America	CENTRAL-AMERICA	38
SEA	South-Eastern-Asia	ASIA	39
SEAF	South-Eastern-Africa	AFRICA	40
SES	South-Eastern South-America	SOUTH-AMERICA	41
SIO	South Indic Ocean	INDIAN	42
SSA	Southern South-America	SOUTH-AMERICA	43
SWS	South-Western South-America	SOUTH-AMERICA	44
TIB	Tibetan-Plateau	ASIA	45
WAF	Western-Africa	AFRICA	46
WCA	West Central Asia	ASIA	47
WCE	West & Central-Europe	EUROPE	48
WNA	Western North-America	NORTH-AMERICA	49
WSAF	W.Southern-Africa	AFRICA	50
WSB	W.Siberia	ASIA	51

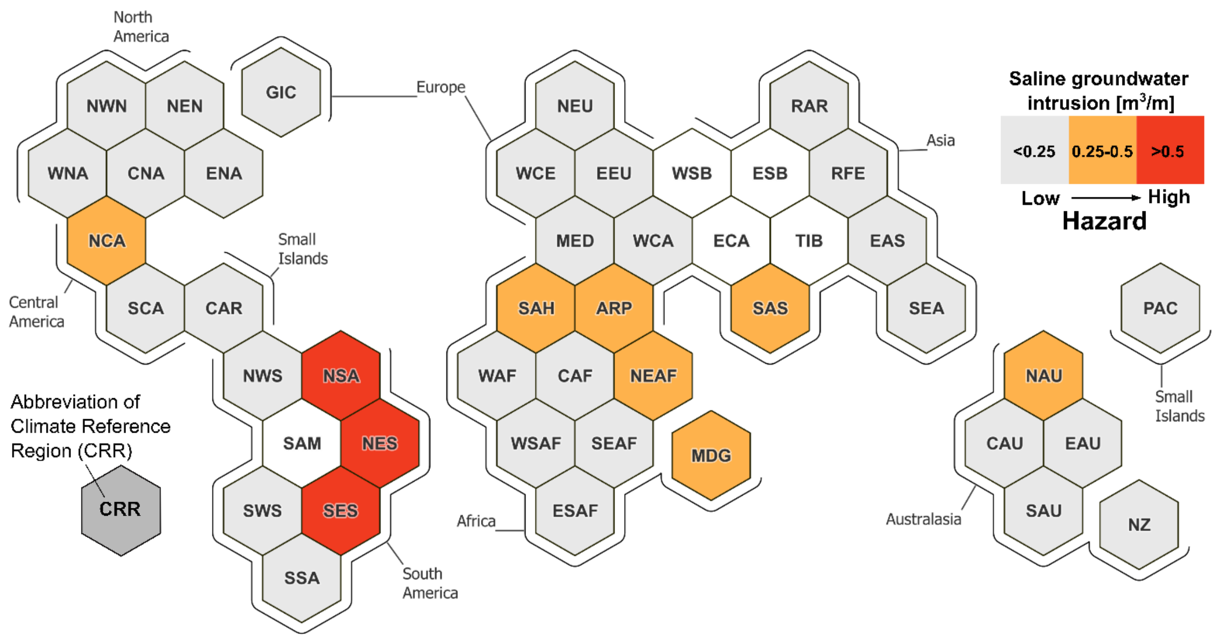

Figure S4 - Simulated climate-driven saline groundwater intrusion per unit length of coastline between 2025 and 2300, aggregated for each climate reference region (for list of abbreviations, see Table S1). White regions are landlocked. Hexagons adapted from ref. [17].

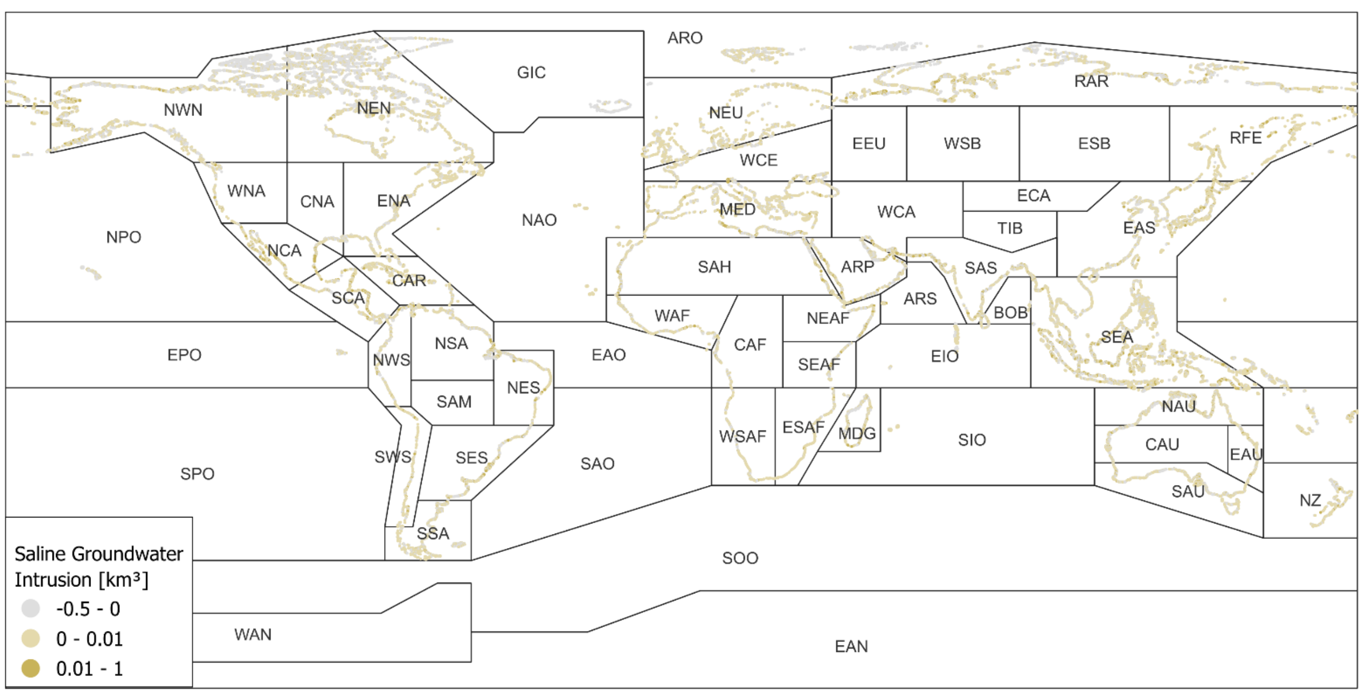

Figure S5 – Volume of climate-driven saline groundwater intrusion in simulated grid cells by 2300 compared to 2025. First, the 2025 and 2300 saline groundwater interface heights were cleaned by subtracting the steady extension simulation results from the transient simulations (i.e., removing interface movement that was still ongoing after the quasi-equilibrium simulated for 1891). Then, the cleaned 2025 interface heights were subtracted from the cleaned 2300 interface heights.

Text S5 – Risk from saltwater intrusion may be increasing in many regions while decreasing in other regions

The hazard, saltwater intrusion, is projected to increase and decrease regionally in the 21st century[12,13]. The decrease in risk is mostly driven by lowering relative sea levels in few climate reference regions far north, inducing a freshening of coastal aquifers. However, for most parts of the world, sea levels are rising in the 21st century. Thus, for most climate reference regions, the delta between 2025 and 2300 is positive: cells are salinizing, increasing the risk. To better understand controlling features, we evaluate regions with saltwater intrusion separately from freshening regions.

We evaluate hazard, exposure, vulnerability and risk at cells in which the saline groundwater content changes between 2025 and 2000/2100/2200/2300.

Text S6 – Random Forest and PAWN

The Random Forest ensemble machine learning method constructs multiple decision trees using bootstrap samples of the data, which we applied to our simulations to quantify the feature importance and feature values that coincide with salinization. The input datasets are features (i.e., input data) and a signal (here: model output). The decision trees are constructed by recursively splitting the dataset into subsets based on the feature and threshold that result in the greatest reduction in impurity (here: Gini impurity). Each split creates two new nodes. At each node, the best split is found by evaluating all possible thresholds for each feature and choosing the one that most effectively separates the signal into homogeneous groups. The feature importance of the random forest is an aggregation of the splits of all trees.

The PAWN method was used to rank the feature sensitivities and to check the plausibility of the random forest results. PAWN is a global, non-parametric sensitivity analysis technique designed to assess the influence of input variables on model outputs. Developed by ref. [18], compares the cumulative distribution function (CDF) of the model output with unconditional CDFs of the output (one unconditional CDF for each input variable). The discrepancy between these CDFs, measured using the Kolmogorov-Smirnov statistic, is interpreted as the sensitivity of the output to the input variables. PAWN is distribution-free and model-agnostic, making it suitable for highly non-linear and non-monotonic models.

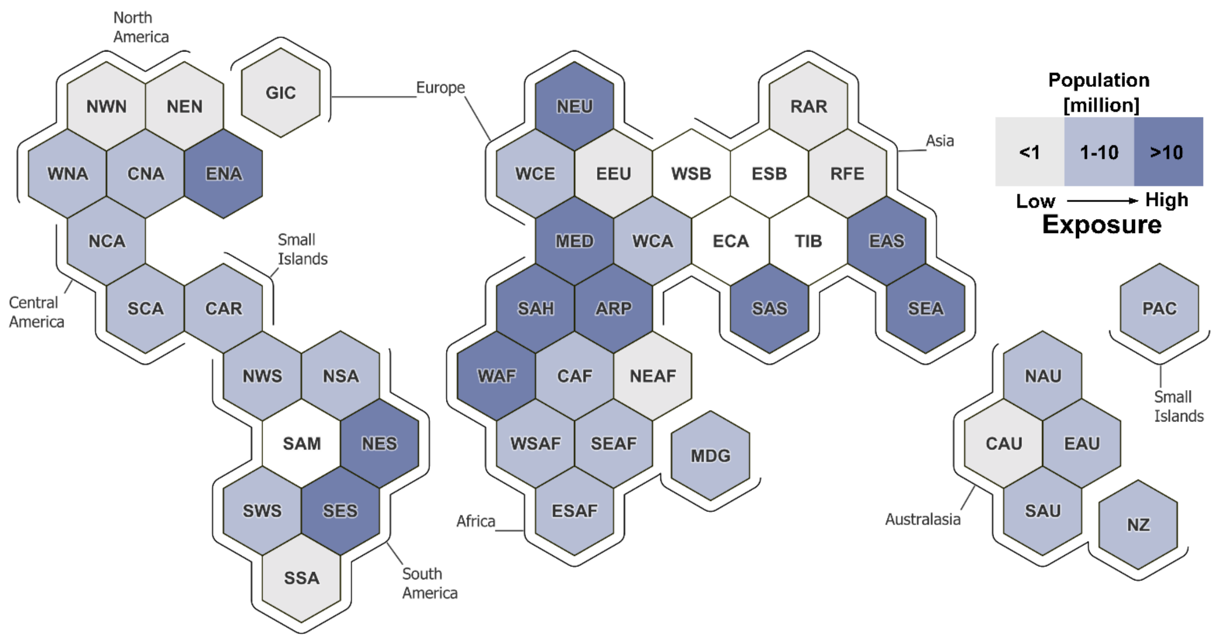

Figure S6 – Estimated population count for 2020[19] aggregated for each climate reference region

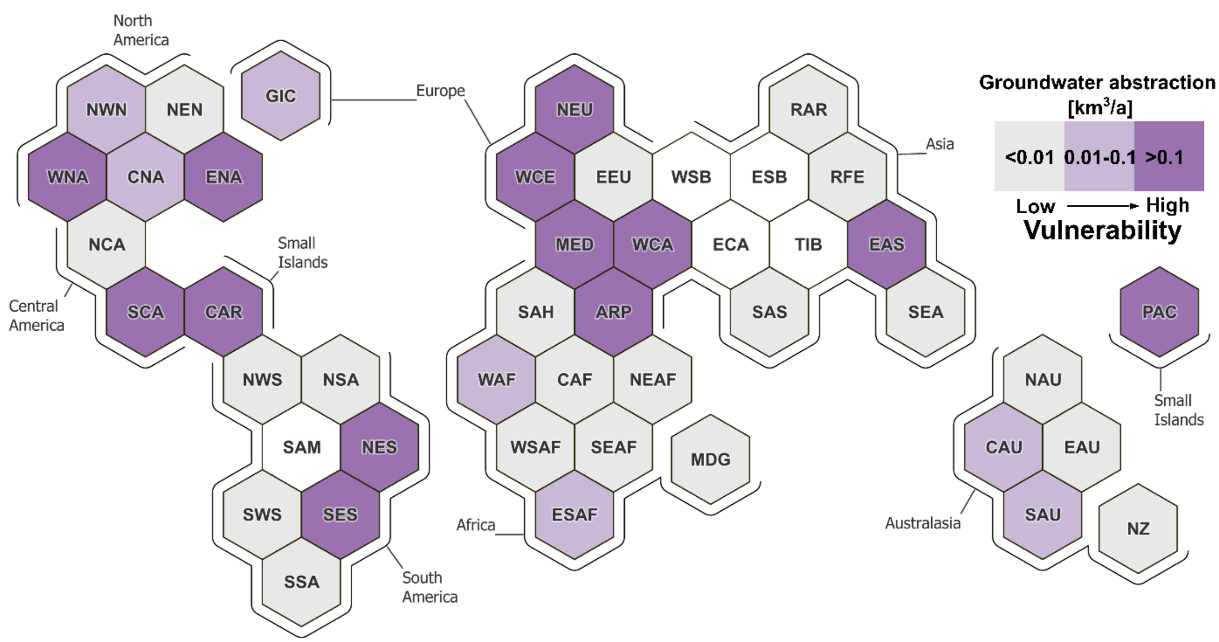

Figure S7 – Estimated mean annual net groundwater abstraction of 2007-2016[9], aggregated for each climate reference region

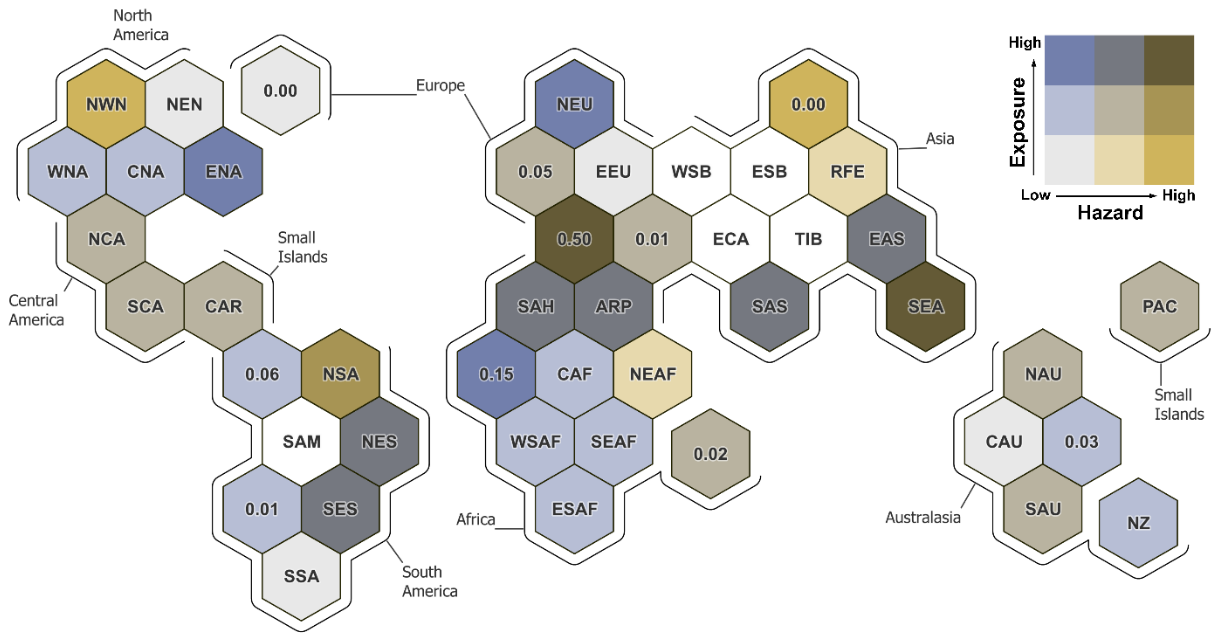

Figure S8 – Bivariate plot of estimated population count for 2020[19] and simulated saltwater intrusion in 2300, aggregated for each climate reference region

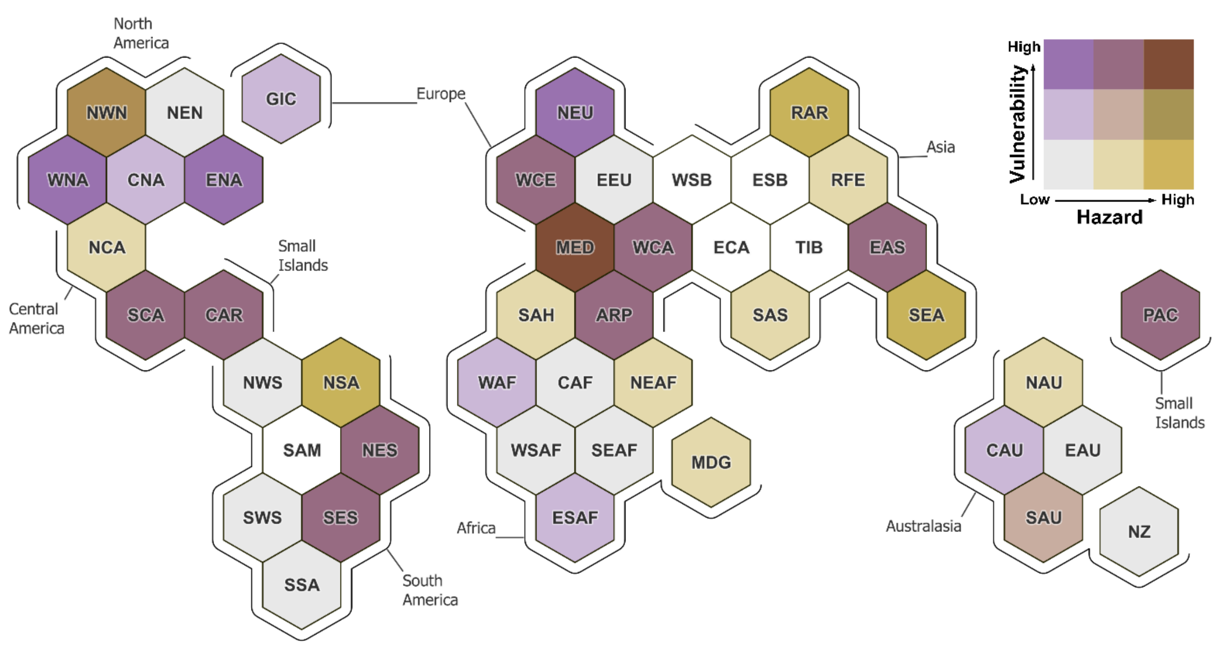

Figure S9 – Bivariate plot of estimated mean annual net groundwater abstraction of 2007-2016[9] and simulated saltwater intrusion in 2300, aggregated for each climate reference region.

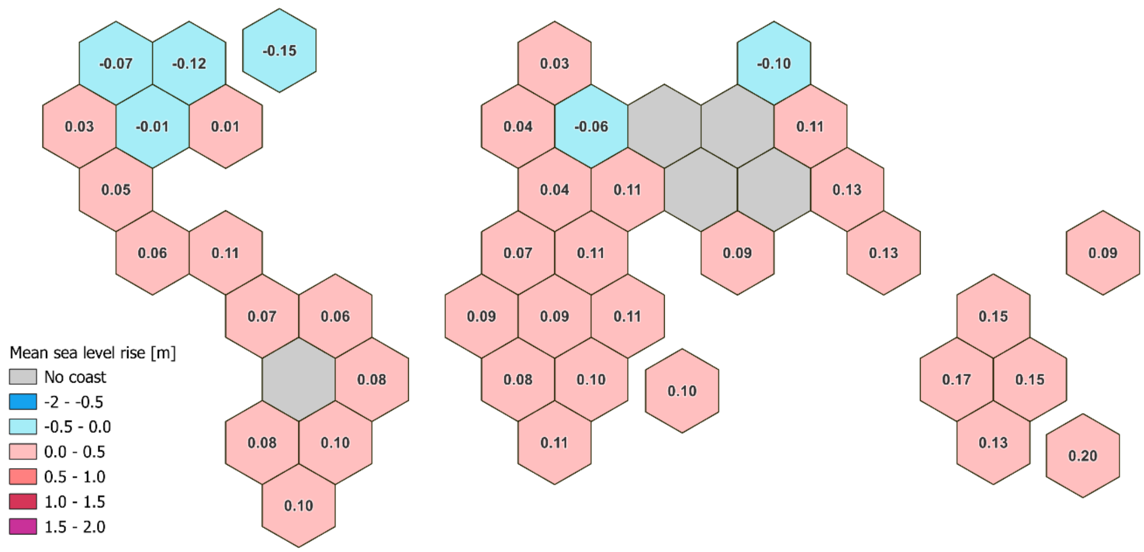

Figure S10 – Mean relative sea level rise in climate reference regions by the year 2000[12,13]

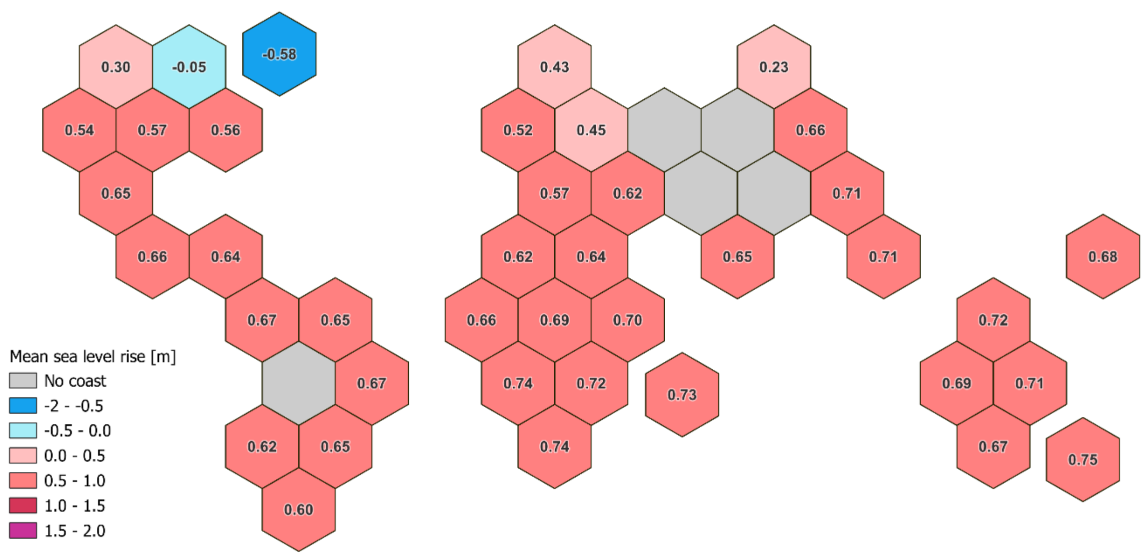

Figure S11 – Mean relative sea level rise in climate reference regions by the year 2100[12,13]

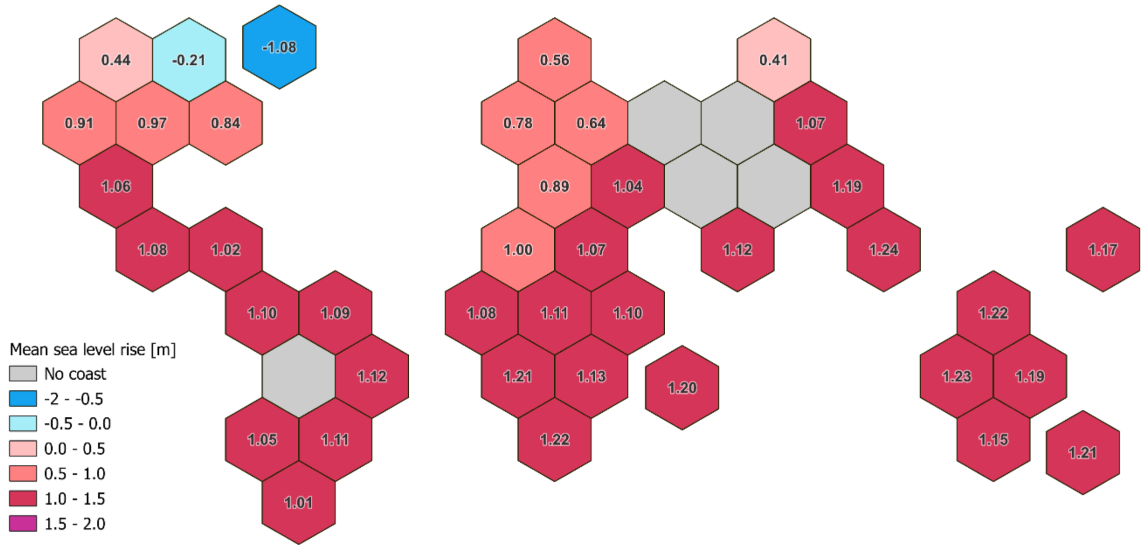

Figure S12 – Mean relative sea level rise in climate reference regions by the year 2200[12,13]

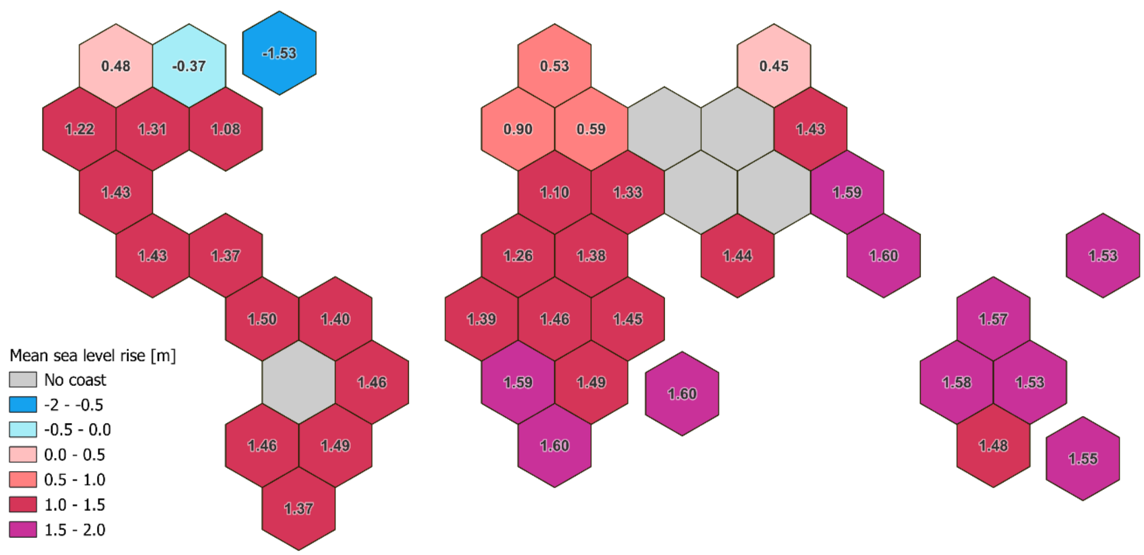

Figure S13 – Mean relative sea level rise in climate reference regions by the year 2300[12,13]

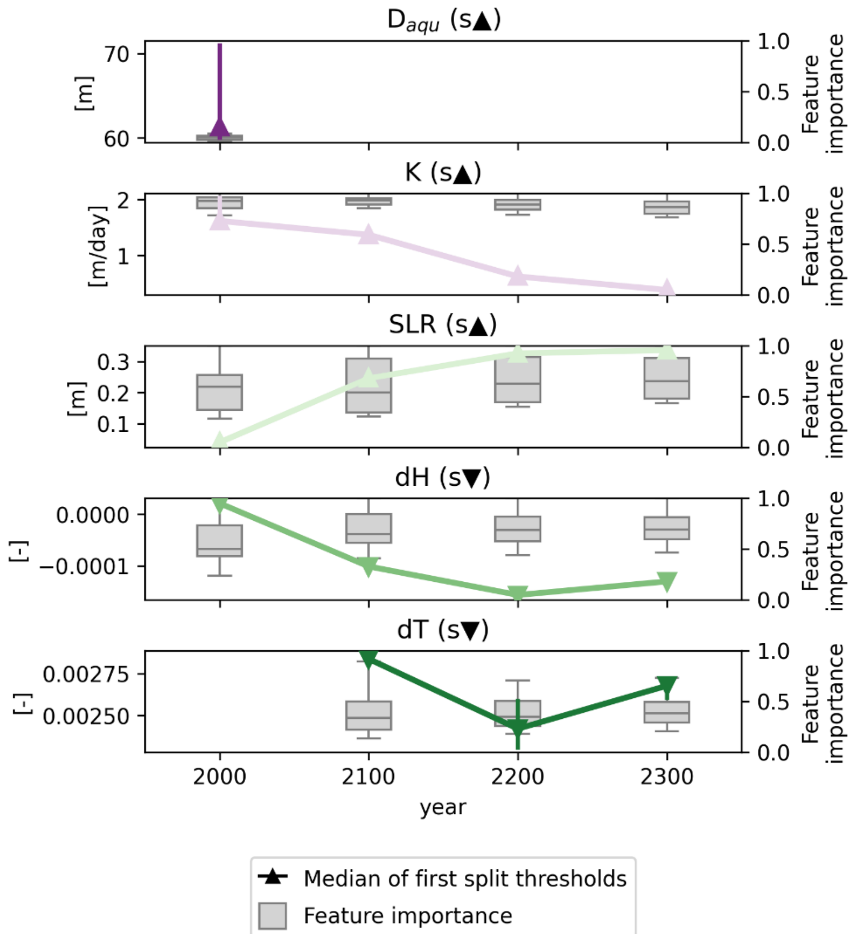

Figure S14 – Feature importance and intrusion thresholds resulting from the random forest algorithm using change in salinity level by 2000, 2100, 2200, and 2300 as signal. Boxes show the feature importance of the model features D_{aqu}, K, SLR, dH and dT. Colored lines show the intrusion thresholds, which are calculated as the median of the random forest first split thresholds. Triangles pointing up/down indicate that above/below the intrusion threshold, groundwater was found to be mainly saline. Model cells with no change in salinity level were omitted in the evaluation. GWRC is not shown as it was identified as the main feature in not a single tree. Compared to Figure 3 in the manuscript, results for D_{aqu} are added here.

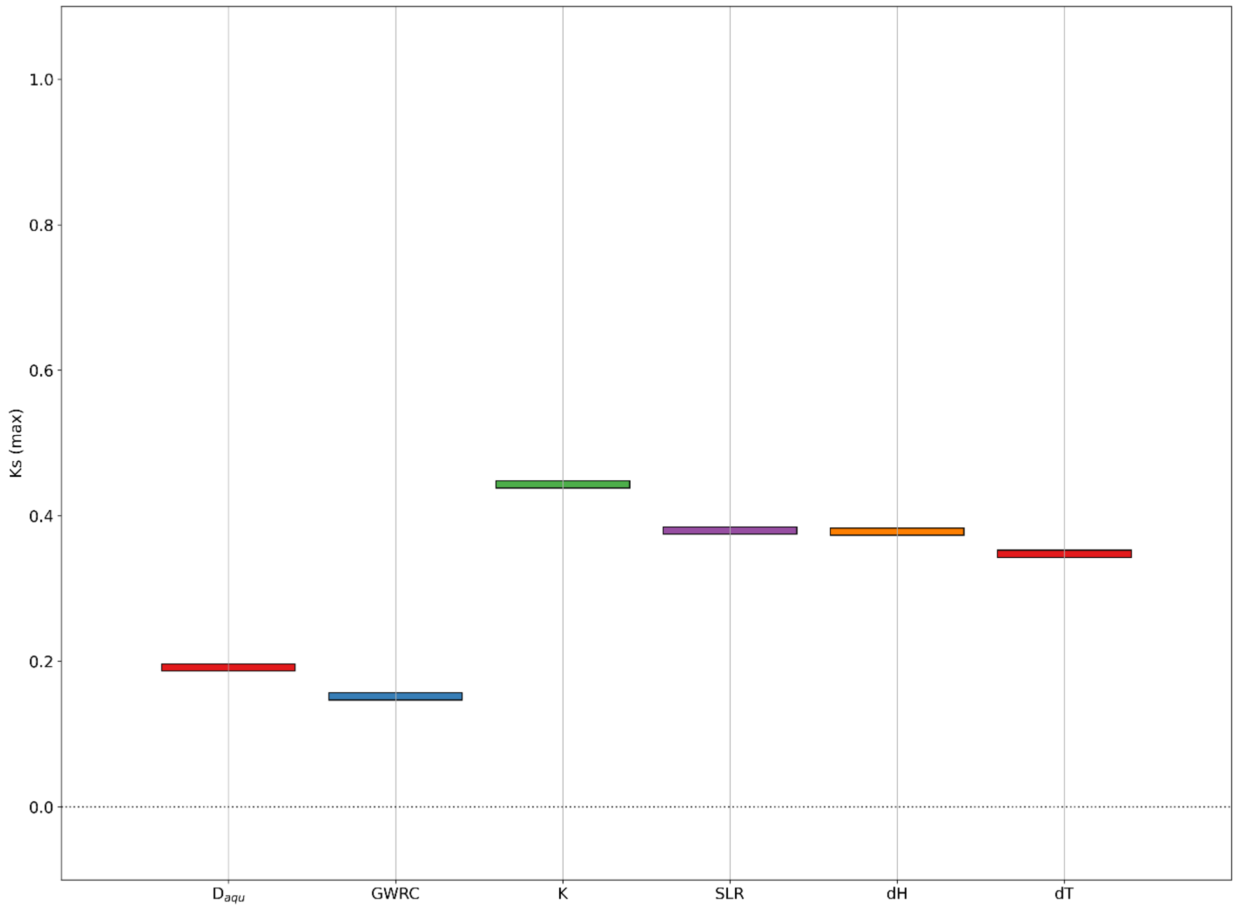

Figure S15 – Results of the PAWN method, using aquifer thickness (D_{aqu}), hydraulic conductivity (K), sea level rise (SLR), groundwater recharge change (GWRC), hydraulic gradient (dH), and topographic gradient (dT) as input variables and change in salinity level by 2300 (vs. 2025) as output variable. Model cells with no change in salinity level were omitted in the evaluation. The analyzed model output, change in salinity level, has highest sensitivity towards hydraulic conductivity (K), followed by sea level rise (SLR), hydraulic gradient (dH) and topographic gradient (dT). Aquifer thickness (D_{aqu}) and groundwater recharge change (GWRC) are not irrelevant, but less influential compared to the top four.

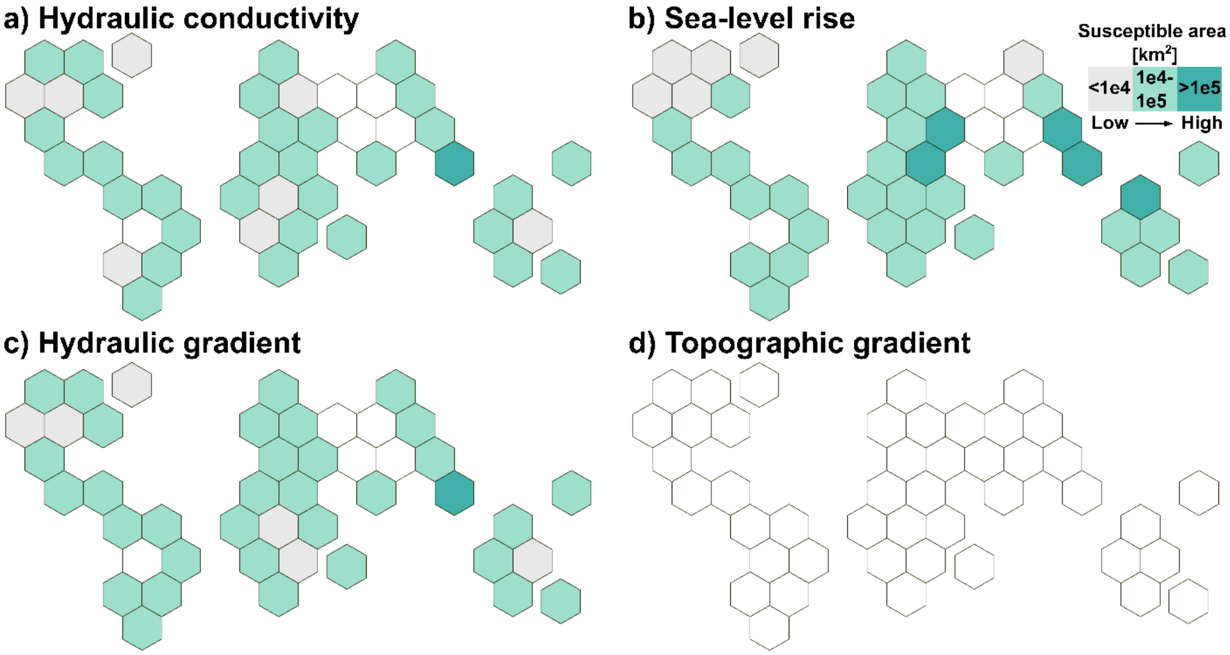

Figure S16 – Coastal area (i.e., < 100 km inland and < 100 m) susceptible to saline groundwater intrusion due to physical factors in climate reference regions in 2000. White regions are landlocked or have no threshold. Colors show the coastal area within the climate reference regions, in which a) hydraulic conductivity (K), b) sea level rise (SLR) are above, and c) hydraulic gradient (dH), d) topographic gradient (dT) are below their intrusion thresholds. Cells that cannot be reached by saline water (i.e., with effective porosity of 0 and cell elevation larger than or equal to aquifer thickness) are included in the evaluation.

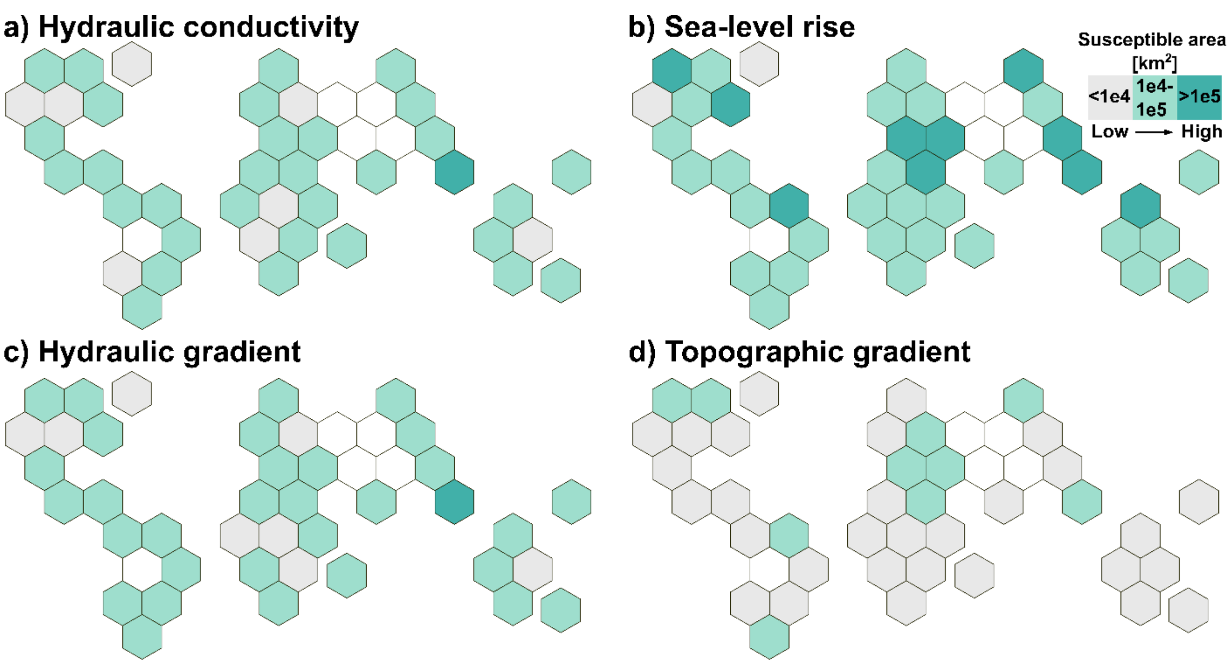

Figure S17 – Coastal area (i.e., < 100 km inland and < 100 m) susceptible to saline groundwater intrusion due to physical factors in climate reference regions in 2100. White regions are landlocked. Colors show the coastal area within the climate reference regions, in which a) hydraulic conductivity (K), b) sea level rise (SLR) are above, and c) hydraulic gradient (dH), d) topographic gradient (dT) are below their intrusion thresholds. Cells that cannot be reached by saline water (i.e., with effective porosity of 0 and cell elevation larger than or equal to aquifer thickness) are included in the evaluation.

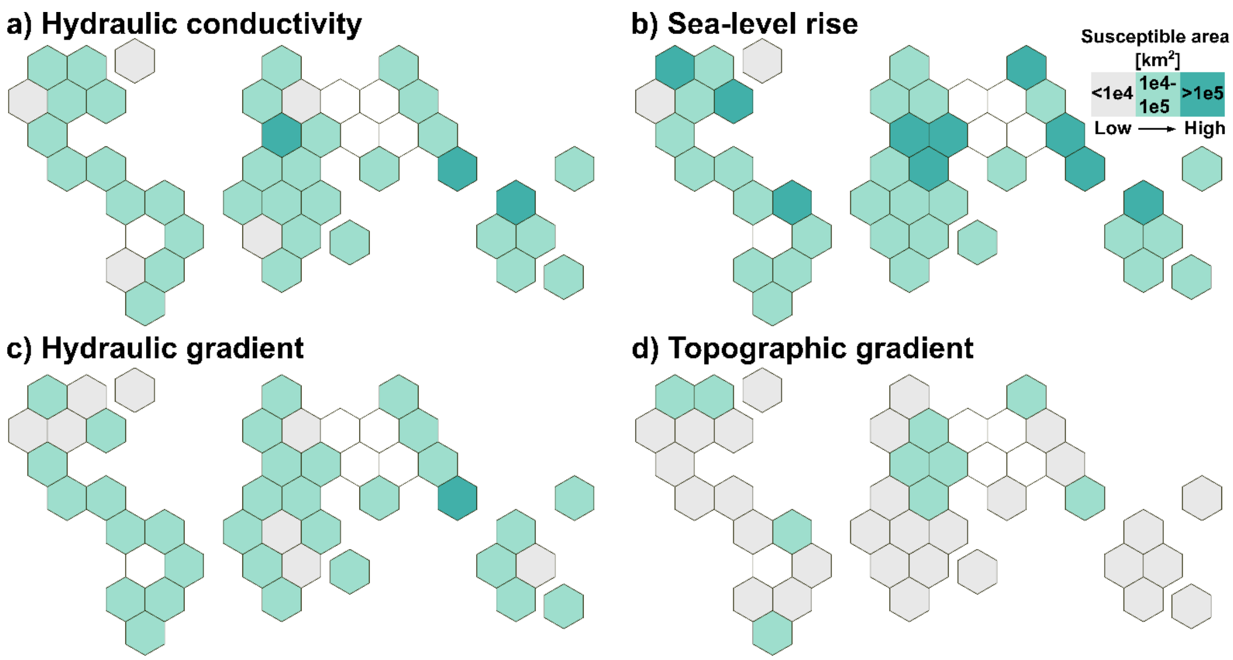

Figure S18 – Coastal area (i.e., < 100 km inland and < 100 m) susceptible to saline groundwater intrusion due to physical factors in climate reference regions in 2200. White regions are landlocked. Colors show the coastal area within the climate reference regions, in which a) hydraulic conductivity (K), b) sea level rise (SLR) are above, and c) hydraulic gradient (dH), d) topographic gradient (dT) are below their intrusion thresholds. Cells that cannot be reached by saline water (i.e., with effective porosity of 0 and cell elevation larger than or equal to aquifer thickness) are included in the evaluation.

Table S2 – Global area susceptible to climate-driven saline groundwater intrusion per feature in 2000, 2100, 2200, and 2300. Areas may overlap. Strong increases in susceptible area are found between 2000-2100 for sea level rise, together with increasing total area susceptible. After 2100, the total area susceptible stagnates, while area susceptible due to hydraulic conductivity and hydraulic gradient are increasing.

	2000 [million km²]	**2100 [million km²]**	**2200 [million km²]**	**2300 [million km²]**
Hydraulic conductivity	1.59	1.62	1.86	1.92
Sea level rise	2.27	2.91	2.89	2.87
Hydraulic gradient	1.11	0.91	0.99	1.08
Topographic gradient	-	0.51	0.51	0.51

Total	2.67	3.06	3.05	3.05

References of Supplement

1. Reinecke, R., Foglia, L., Mehl, S., Herman, J. D., Wachholz, A., Trautmann, T. & Döll, P. Spatially distributed sensitivity of simulated global groundwater heads and flows. *Hydrology and Earth System Sciences* **23**, 4561–4582 (2019).

2. Reinecke, R., Foglia, L., Mehl, S., Trautmann, T., Cáceres, D. & Döll, P. Challenges in developing a global gradient-based groundwater model. *Geoscientific Model Development* **12**, 2401–2418 (2019).

3. Harbaugh, A. W. MODFLOW-2005, the U.S. Geological Survey modular groundwater model – the Ground-Water Flow Process. *U.S. Geological Survey Techniques and Methods* 6-A16, 2005.

4. Bakker, M., Schaars, F., Hughes, J. D., Langevin, C. D. & Dausman, A. M. Documentation of the Seawater Intrusion (SWI2) Package for MODFLOW. *U.S. Geological Survey Techniques and Methods* **6**, chap. A46 (2013).

5. Kretschmer, D. V., Michael, H. A., Moosdorf, N., Oude Essink, G. H. P., Bierkens, M. F. P., Wagener, T. & Reinecke, R. Controls on coastal saline groundwater across North America. *Environmental Research Letters* **20**, 024065 (2025).

6. Oppenheimer, M., Glavovic, B. C., Hinkel, J., van de Wal, R., Magnan, A. K., Abd-Elgawad, A., Cai, R., Cifuentes-Jara, M., DeConto, R. M., Ghosh, T., Hay, J., Isla, F., Marzeion, B., Meyssignac, B. & Sebesvari, Z. Sea level rise and implications for low-lying islands, coasts and communities. In *IPCC Special Report on the Ocean and Cryosphere*, 321–445 (Cambridge University Press, 2019).

7. Huscroft, J., Gleeson, T., Hartmann, J. & Börker, J. Compiling and Mapping Global Permeability of the Unconsolidated and Consolidated Earth: GLobal HYdrogeology MaPS 2.0 (GLHYMPS 2.0). *Geophysical Research Letters* **45**, 1897–1904 (2018).

8. Reinecke, R., Müller Schmied, H., Trautmann, T., Andersen, L. S., Burek, P., Flörke, M., Gosling, S. N., Grillakis, M., Hanasaki, N., Koutroulis, A., Pokhrel, Y., Thiery, W., Wada, Y., Yusuke, S. & Döll, P. Uncertainty of simulated groundwater recharge at different global warming levels: a global-scale multi-model ensemble study. *Hydrology and Earth System Sciences* **25,** 787-810 (2021).

9. Müller-Schmied, H. *et al.* The global water resources and use model WaterGAP v2.2d. PANGAEA https://doi.org/10.1594/PANGAEA.918447 (2020).

10. Shangguan W., Hengl T., Mendes J. J., Yuan H. & Dai Y. Mapping the global depth to bedrock for land surface modeling. *Journal of Advances in Modeling Earth Systems* **9**, 65-88 (2017).

11. Moosdorf N., Tschaikowski, J., Kretschmer, D. & Reinecke, R. A global coastal permeability dataset (CoPerm 1.0). *Scientific Data*, **11**, 893 (2024).

12. Mengel, M., Levermann, A., Frieler, K., Robinson, A., Marzeion, B. & Winkelmann, R. Future sea level rise constrained by observations and long-term commitment. *Proceedings of the National Academy of Sciences USA* **113**, 2597–2602 (2016).

13. Mengel, M. ISIMIP2b sea-level rise input data (v1.0). ISIMIP Repository https://doi.org/10.48364/ISIMIP.768189 (2017).

14. Feth J. H. Preliminary Map of the Conterminous United States Showing Depth to and Quality of Shallowest Ground Water Containing More Than 1,000 Parts Per Million Dissolved Solids: Hydrologic Investigations Atlas HA-199, 31 p., 1965.

15. Reilly T. E., Dennehy, K. F., Alley, W. M. & Cunningham W. L. Ground-Water Availability in the United States: U.S. *Geological Survey Circular* **1323**, 70 p., (2008).

16. Iturbide, M. *et al.* An update of IPCC climate reference regions for subcontinental analysis of climate model data. *Earth System Science Data* **12**, 2959–2970 (2020).

17. IPCC. Summary for Policymakers. In *Climate Change 2021: The Physical Science Basis*, 3–32 (Cambridge University Press, 2021).

18. Pianosi, F. & Wagener, T. Distribution-based sensitivity analysis from a generic input-output sample. *Environmental Modelling & Software* **108**, 197–207 (2018).

19. Center for International Earth Science Information Network (CIESIN). *Documentation for the Gridded Population of the World, Version 4 (GPWv4), Revision 11 Data Sets* (2018).